

Curvilinear Finite Volume Schemes using High Order Compact Interpolation

Arnaud Fosso P.^a, Hugues Deniau^a, Frédéric Sicot^a, Pierre Sagaut^b

^a*CERFACS Advanced Aerodynamic and Multiphysics Department*

^b*Institut Jean Le Rond d'Alembert, Université Pierre et Marie Curie - UPMC, 4 place Jussieu - case 162, F-75252 Paris cedex 5, France*

Abstract

During the last years, the need of high fidelity simulations on complex geometries for aeroacoustics predictions has grown. Most of high fidelity numerical schemes, in terms of low dissipative and low dispersive effects, lie on Finite-Difference (FD) approach. But for industrial applications, FD schemes are less robust compared to Finite-Volume (FV) ones. Thus the present study focuses on the development of a new compact FV scheme for two- and three- dimensional applications.

The proposed schemes are formulated in the physical space and not in the computational space as it is the case in most of the known works. Therefore, they are more appropriate for general grids. They are based on compact interpolation to approximate interface-averaged field values using known cell-averaged values. For each interface, the interpolation coefficients are determined by matching Taylor series expansions around the interface center. Two types of schemes can be distinguished. The first one uses only the curvilinear abscissa along a mesh line to derive a sixth-order compact interpolation formulae while the second, more general, uses coordinates in a spatial three-dimensional frame well chosen. This latter is formally sixth-order accurate in a preferred direction almost orthogonal to the interface and at most fourth-order accurate in transversal directions. For non-linear problems, different approaches can be used to keep the high-order scheme. However, in the present paper, a MUSCL-like formulation was sufficient to address the presented test cases.

All schemes have been modified to treat multiblock and periodic interfaces in such a way that high-order accuracy, stability, good spectral resolution, conservativeness and low computational costs are guaranteed. This is a first step to insure good scalability of the schemes although parallel performances issues are not addressed. As high frequency waves, badly resolved, could be amplified and then destabilize the scheme, compact filtering operators have been used.

Numerous test cases as the linear convection of a gaussian wave, the convection of a Lamb-Oseen vortex and the diffraction of an acoustic wave on a plane have been realized to validate the schemes. The most efficient schemes are shown to be at least fifth-order accurate on linear and non-linear convection problems. They are also less dissipative and less dispersive on non-uniform curvilinear grids than schemes using implicit interpolation with constant coefficients of the same order on uniform cartesian grids.

Key words: Finite-volume, high order scheme, compact interpolation, multiblock computations, stability analysis, aeroacoustics

11 The use of computational fluid dynamics (CFD) methods in computational aeroacoustics (CAA) to
12 address noise generation and propagation problems is now a well established practice in engineering.
13 However it is well known that CFD methods must be modified in order to satisfy stringent requirements
14 of CAA [23]. Indeed, aeroacoustics problems generally display an unsteady behaviour, a broad and
15 disparate spectral bandwidth along with a large-magnitude disparity between the mean and acoustic flow
16 quantities. Thus, important efforts have been done to realize numerical schemes higher-order accurate, low
17 dissipative and low dispersive.

18 Numerous studies have contributed to improve numerical tools for aeroacoustic computation but
19 almost entirely in Finite-Difference (FD) framework. The main ideas of those works are illustrated
20 by the Tam and Webb [25] dispersion relation preserving (DRP) scheme and the Padé-like compact
21 schemes [14]. These methods exhibit an improved spectral resolution while having the same accuracy as
22 the standard explicit methods of the same order. One can find abundant literature on the application
23 of these methods on arbitrary meshes always in the finite-difference (FD) context [5, 26].

24 However Finite-Volume (FV) formulations are generally preferred for industrial applications due to
25 their robustness. Indeed, they are based on the weak formulation of the field equations and so require less
26 smoothness of functions or mesh than FD formulations. Furthermore, FV methods are advantageous
27 since they allow to satisfy the governing conservation laws of the fluid physics. Actually, it is shown
28 in Mattiussi [15], using algebraic topology concepts, that integral methods like FV and FE (Finite
29 Element) methods are more suitable for field equations than FD methods. Therefore, the need of high-
30 order accurate and low dissipative and low dispersive FV schemes on arbitrary grids is certain, and the
31 present study is in line with this approach.

32 Efforts have been done to extend both DRP and compact schemes approaches to FV context. For
33 example, Gaitonde and Shang [3] introduced a class of fourth-order finite volume compact schemes for
34 linear problems. Kobayashi [12] extends this work by analyzing general implicit interpolation schemes.
35 Nance et al. [16] proposed a way to set up explicit interpolation which satisfies the DRP property to
36 calculate rotorcraft noise. Recently, Popescu et al. [21] adapted DRP scheme of Tam and optimized
37 prefactored compact schemes of Ashcroft and Zhang [1] and Hixon [10] to obtain high-order, low dis-
38 sipative and dispersive FV schemes. But all these works deal with uniform grids. Pereira et al. [17]
39 performed computations for incompressible Navier-Stokes equations using a fourth-order compact FV
40 scheme. They extend the scheme to arbitrary grids using transformed coordinates. The same approach
41 has been used in the recent work of Piller and Stalio [18, 19]. They take into account that, in FV
42 context, cell-averaged values are known and in particular they do not use these value as pointwise values
43 at cells centers. Lacor et al. [13] proposed a compact interpolation of values on cell interfaces in the
44 physical space and these values are used to determine the fluxes. This interpolation is made by directly
45 accounting for multidimensional derivatives involving in the Taylor series expansion of the function to
46 interpolate. The scheme obtained were fourth-order accurate on regular grids and second order accurate
47 on arbitrary grids. This approach is well suited for highly irregular grids.

48 This study is in line with the one of Lacor and coworkers. The proposed schemes allow to reach,
 49 on average, the fifth-order accuracy on regular meshes (even curvilinear) and the spectral resolution of
 50 commonly used FD compact schemes on a cartesian uniform mesh. To do that, they use sixth-order
 51 compact interpolation to compute values on interfaces. The schemes explicitly care that there are cell-
 52 averaged values which are used in a FV context. Two types of schemes can be distinguished. The first
 53 type uses curvilinear abscissa assuming that the problem is unidimensional (1D) along the curvilinear
 54 line between the centers of interfaces on a given mesh line. Therefore, values on interfaces are considered
 55 as values at the center of the interface and cell-averaged values are line-averaged values. The second one
 56 is more general since it takes into account that values needed on interfaces are interface-averaged values.
 57 So they are line-averaged values in 2D and surface-averaged values in 3D. And cell-averaged values are
 58 surface-averaged values in 2D and volume-averaged values in 3D. Therefore the Taylor expansion series
 59 used to find the interpolation formulae involves multidimensional derivatives.

60 For aeroacoustics computations, even if the numerical scheme has good properties in terms of dis-
 61 sipation and dispersion, the grid must be fine enough to resolve well either the turbulent structures
 62 which are the noise source, and the convection of acoustic wave with a sufficient number of points per
 63 wave-length. The number of points is generally so important that computations have to be done with a
 64 parallel multiblock strategy. Thus the proposed schemes have to be adapted for multiblock computations
 65 and this issue is carefully adressed. Since it is shown that all boundary treatments can create spurious
 66 high frequency waves numerical, stabilization procedures are also considered.

67 The paper is organized as follows. In section 2, the two types of interior schemes are detailed. After
 68 a rapid recall about how a scheme could be studied with the matrix method in section 2.4, multiblock
 69 and periodic boundary closures are discussed in section 2.5. In Section 3 are reported some remarks
 70 specific to the non-linear case. Section 4 gives a rapid view about filtering operators used. Then some
 71 numerical tests are performed in Section 5. Firstly, a numerical study is done on a linear convection
 72 problem in section 5.1. Then, a non linear case which consists in the convection of a vortex, is presented
 73 in section 5.2. Finally, to highlight the high accuracy and the good spectral properties of the schemes,
 74 a benchmark acoustic problem is solved in section 5.3 on an irregular mesh using a non-linear code.

75 2. Finite Volume method and high-order compact interpolations

76 Let be considered the following linear convection equation:

$$\frac{\partial u}{\partial t} + \nabla \cdot \mathbf{f}(u) = 0, \quad (1)$$

77 where $\mathbf{f}(u)$ is a linear vectorial function of u . By integrating Eq. (1) over a volume control Ω and using
 78 the Stokes formula, one can obtain:

$$V \frac{d\bar{u}}{dt} + \oint_{\partial\Omega} \mathbf{f}(u) \cdot \mathbf{n} dS = 0, \quad (2)$$

79 with $V = |\Omega|$ and

$$\bar{u} = \frac{1}{V} \int_{\Omega} u d\Omega.$$

80 Now, it is assumed that Ω is a polyhedron (polygon in 2D), *i.e.* the unitary normal on each of its faces
81 is constant over the face. Therefore, using the linearity of \mathbf{f} , Eq. (2) leads to:

$$V \frac{d\bar{u}}{dt} + \sum_{i=1}^{n_f} \mathbf{f} \left(\int_{\partial\Omega_i} u dS \right) \cdot \mathbf{n}_i = 0, \quad (3)$$

82 where n_f is the number of faces and $\partial\Omega_i$, the i -th face of Ω . Eq. (3) is equivalent to

$$V \frac{d\bar{u}}{dt} + \sum_{i=1}^{n_f} \mathbf{f}(\bar{u}_i) S_i \cdot \mathbf{n}_i = 0, \quad (4)$$

83 where $S_i = |\partial\Omega_i|$ and

$$\bar{u}_i = \frac{1}{S_i} \int_{\partial\Omega_i} u dS.$$

84 Hence, to obtain a high-order discretization of Eq. (4), it is sufficient to have a high-order approximation
85 of the face-averaged quantity \bar{u}_i .

86 Now, a three-dimensional structured (indexed by (i, j, k)) grid composed of polyhedrons is considered.
87 This section presents the different strategies proposed to approximate at a high order the interface-
88 averaged value of a quantity u on the interface $(i + 1/2, j, k)$, using cell-averaged values of neighbouring
89 cells. In this section, the mesh line (j, k) for which these two indexes remain constant is under consider-
90 ation. To make this approximation spatially implicit or compact, the formula involves averaged values
91 on neighbouring interfaces $(i - 1/2, j, k)$ and $(i + 3/2, j, k)$. Thus the compact interpolation reads as

$$\alpha \bar{u}_{i-1/2,j,k} + \bar{u}_{i+1/2,j,k} + \beta \bar{u}_{i+3/2,j,k} = \sum_{l=-m}^{l=n} \sum_{p=-q}^{p=r} \sum_{s=-t}^{s=u} a_{l,p,s} \bar{u}_{i+l,j+p,k+s}, \quad (5)$$

92 where

$$\bar{u}_{i,j,k} = \frac{1}{V_{i,j,k}} \int_{V_{i,j,k}} u dV, \quad (6)$$

93 are cell-averaged values and

$$\bar{u}_{i+1/2,j,k} \approx \frac{1}{S_{i+1/2,j,k}} \int_{S_{i+1/2,j,k}} u dS, \quad (7)$$

94 approximate interface-averaged values. The interpolation coefficients α , β and $a_{l,p,s}$ are chosen, depend-
95 ing on the interface $(i + 1/2, j, k)$, in order to obtain a given order of approximation.

96 The system of equations formed with Eq. (5) along the mesh line (j, k) to compute values at the interfaces
97 is a tridiagonal system. This choice has been made since this system is efficiently inverted using, for
98 example, the Thomas algorithm. Moreover, the inversion of the system could be done for each grid line
99 in each dimension.

100 To determine the interpolation coefficients, a Taylor series expansion is done for each term in Eq. (5),
101 and two possibilities are studied in this paper depending on the following choice:

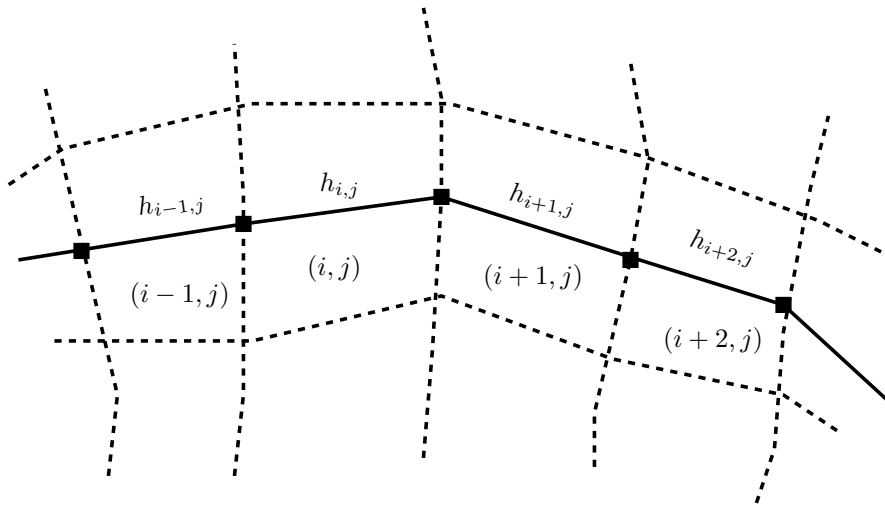


Figure 1: Cartesian-like scheme using curvilinear distances between interfaces.

- 102 • u is considered as a function of s , the curvilinear abscissa along the (j, k) line;
- 103 • u is considered as a function in a well chosen tridimensional coordinates system (x', y', z') .

104 2.1. Cartesian-like scheme using curvilinear abscissa

105 In this section, u is assumed to be a function just of the curvilinear abscissa s along (j, k) -line. Such
 106 a scheme will be referred to as a cartesian-like scheme in the following.

107 To obtain a formally sixth-order scheme, Eq. (5) can be reduced as follows:

$$\alpha \tilde{u}_{i-1/2,j,k} + \tilde{u}_{i+1/2,j,k} + \beta \tilde{u}_{i+3/2,j,k} = a \bar{u}_{i-1,j,k} + b \bar{u}_{i,j,k} + c \bar{u}_{i+1,j,k} + d \bar{u}_{i+2,j,k}. \quad (8)$$

108 A Taylor series expansion of $u(s)$ about the center of the interface $(i + 1/2, j, k)$ is done for all terms in
 109 Eq. (8). In order to get the sixth order, it is necessary to match left and right hand sides coefficients of
 110 successive derivatives ∂s^q up to the fifth order. So, six equations are obtained, and coefficients α , β , a ,
 111 b , c and d , are explicitly found as functions of the distances between interfaces (Fig. 1) which represent
 112 the curvilinear abscissae. (see details in Appendix A).

113 For an uniform grid, one can find the following interpolation formula:

$$\frac{1}{3} \tilde{u}_{i-1/2,j,k} + \tilde{u}_{i+1/2,j,k} + \frac{1}{3} \tilde{u}_{i+3/2,j,k} = \frac{1}{36} \bar{u}_{i-1,j,k} + \frac{29}{36} \bar{u}_{i,j,k} + \frac{29}{36} \bar{u}_{i+1,j,k} + \frac{1}{36} \bar{u}_{i+2,j,k}. \quad (9)$$

114 However, this scheme does not account for the variation of the cells and interfaces shapes and for the
 115 curvature of mesh lines. This deficiency is corrected by a more general approach presented in the next
 116 section.

117 2.2. General curvilinear scheme

118 In the general case, since u is a function of three coordinates x, y, z for three-dimensionnal flow,
 119 the Taylor series expansion introduced in Eq. (5) involves all derivatives with respect to these three

Derivatives		Total number
1D	$\partial^{(0)}, \partial_{x^i}^{(i)}, i = 1, \dots, 5$	6
2D	$\partial^{(0)}, \partial_{x^i y^j}^{(i+j)}, i, j \in \{0, \dots, 5\}, i + j \leq 5$	21
3D	$\partial^{(0)}, \partial_{x^i y^j z^k}^{(i+j+k)}, i, j, k \in \{0, \dots, 5\}, i + j + k \leq 5$	56

Table 1: Derivatives to cancel out in order to get a formal sixth-order interpolation in all directions.

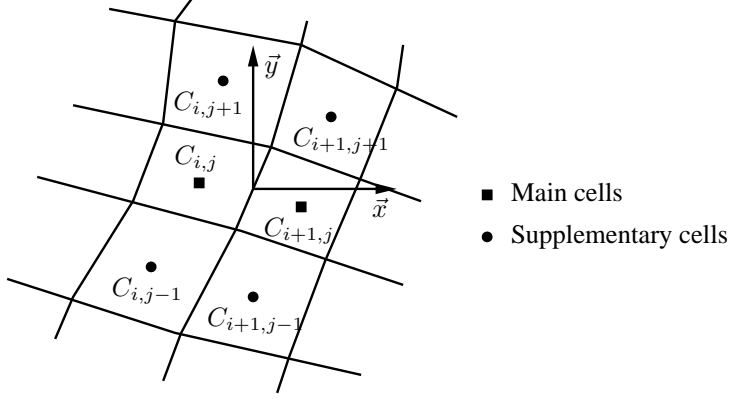


Figure 2: Cells used by Lacor et al. for the curvilinear interpolation.

120 directions:

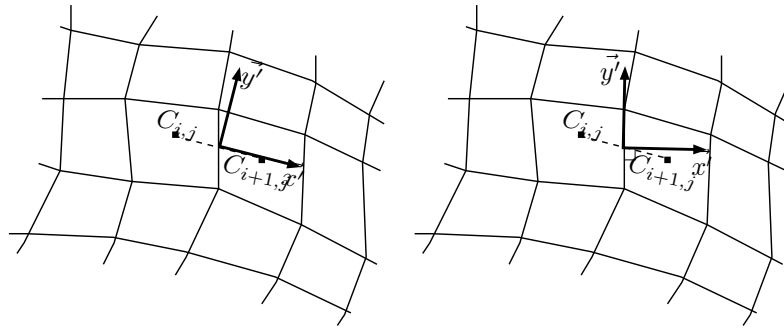
$$u(x, y, z) = \sum_{m=0}^{\infty} \sum_{n=0}^{\infty} \sum_{p=0}^{\infty} \frac{1}{m!} \frac{1}{n!} \frac{1}{p!} (x - x_0)^m (y - y_0)^n (z - z_0)^p \frac{\partial^{m+n+p} u}{\partial x^m \partial y^n \partial z^p} (x_0, y_0, z_0). \quad (10)$$

121 Remembering that averaged values as defined by Eq. (6) and Eq. (7) are considered, relations obtained
 122 using the Taylor series expansion involve kinetic moments $J_{\Omega}^{x^m y^n z^p} = \int_{\Omega} (x - x_{\Omega})^m (y - y_{\Omega})^n (z - z_{\Omega})^p d\Omega$
 123 of cells and interfaces which belong to the stencil (see Appendices B and C for details).

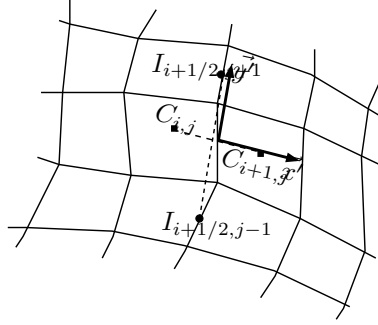
124 In the two dimensional case, there are 21 relations to satisfy in order to get a sixth-order scheme (see
 125 Tab. 1) and it would be too expensive to use a suitable stencil to fulfill these relations.

126 In a previous study, Lacor et al. [13] proposed to use supplementary cells above and below the
 127 interface (see Fig. 2) to obtain a fourth-order scheme. As the number of coefficients was still not
 128 sufficient (8 coefficients for 10 equations to obtain the fourth order), they proposed, in a second step to
 129 obtain a formally third-order accurate scheme (six equations) by imposing all the derivatives up to the
 130 second order to be cancelled out and minimizing the third derivatives coefficients with a least square
 131 method. Since this method leads to unstable simulations, they reduced the formal order to two and set
 132 $\alpha = \beta = 1/4$ which are the values obtained to get the fourth-order accuracy on an uniform grid.

133 The general compact FV approach proposed in the present work also relies on the use of supplementary
 134 cells above and below the interface and a least square approach to account for their contribution. But
 135 it differs from Lacor's method on some important points. The main idea lies in the definition of a
 136 new frame, local to each interface, in which the Taylor series expansions are performed. Since only the



(a) Orthogonal frame defined by the cell centers line. (b) Orthogonal frame defined by the normal of the interface.



(c) Non orthogonal frame defined by the cell centers lines.

Figure 3: Different local frames considered for the high-order curvilinear interpolation.

137 interfaces $(i - 1/2, j, k)$, $(i + 1/2, j, k)$ and $(i + 3/2, j, k)$ appear in Eq. (5), the proposed scheme has
 138 already a preferred direction along this (j, k) -line. Thus a new frame (x', y', z') is introduced so that
 139 the x' -direction represents this preferred direction, tangent to (j, k) mesh line. Taylor series expansions
 140 are written in this frame, and all derivatives along x' are cancelled out in order to get the sixth-order
 141 accuracy in this direction. Transverse derivatives along y' and z' are accounted for as corrections terms
 142 using a least square approach. Before presenting these so called transverse correction, the local frame
 143 definition is adressed.

144 2.2.1. Local reference frame

145 Three types of local frames have been considered. The first and second type are orthogonal and differ
 146 by the definition of the preferred direction x' . For the first type, this direction is defined as the direction
 147 given by the centers of the two cells adjacent to the central interface of the stencil (see Fig. 3(a)). For
 148 the second one, the x' direction is defined as the normal to the central interface (Fig. 3(b)). For both
 149 types, the two other directions are built as two independant vectors in the plane normal to x' .
 150 The third frame is non-orthogonal. Its x' axis is chosen as for the first type, the y' and z' directions
 151 correspond to the mesh lines which link the interface center in j and k directions as presented on Fig. 3(c).
 152 The y' direction corresponds to the line which joins the $I_{i+1/2,j+1}$ and $I_{i+1/2,j-1}$ points ($I_{i+1/2,j}$ is the
 153 center of the $S_{i+1/2,j}$ interface). The relevance of this frame will clearly appear when the discretization
 154 stencil will be shown.

Dimension	Derivatives	Total number
2D	$\partial^{(0)}, \partial x', \partial^2 x'^2, \partial^3 x'^3, \partial^4 x'^4, \partial^5 x'^5,$ $\partial y', \partial^2 y'^2, \partial^2 x' y', \partial^3 y'^3, \partial^3 x'^2 y', \partial^3 x' y'^2$	12
3D	$\partial^{(0)}, \partial x', \partial^2 x'^2, \partial^3 x'^3, \partial^4 x'^4, \partial^5 x'^5,$ $\partial y', \partial z', \partial^2 y'^2, \partial^2 z'^2, \partial^2 x' y', \partial^2 x' z', \partial^2 y' z', \partial^3 y'^3, \partial^3 z'^3,$ $\partial^3 x'^2 y', \partial^3 x' y'^2, \partial^3 x'^2 z', \partial^3 x' z'^2, \partial^3 y'^2 z', \partial^3 y' z'^2, \partial^3 x' y' z'$	22

Table 2: Derivatives used for the general curvilinear scheme.

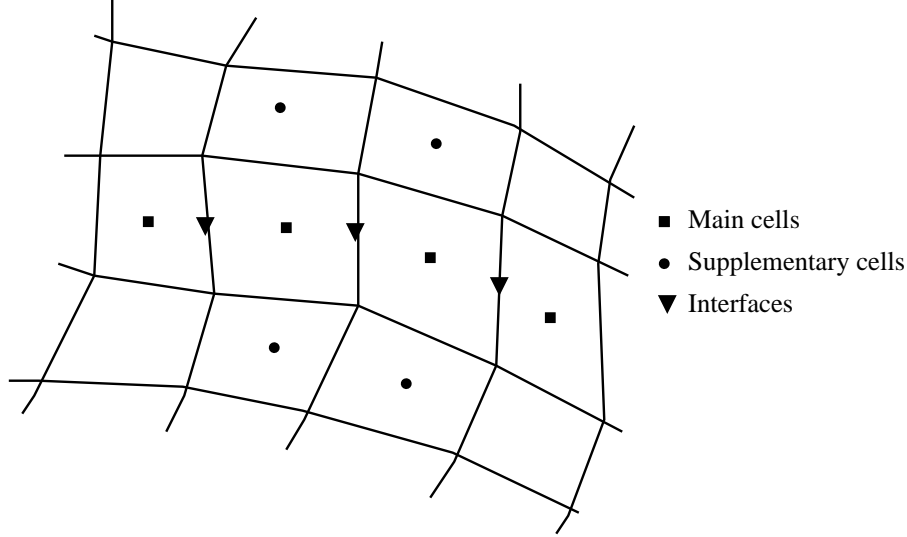


Figure 4: Cells used by the curvilinear interpolation.

155 2.2.2. Transverse derivatives and discretization stencil

156 Since it is too expensive to extend the stencil so that all transverse derivatives are cancelled, it was
157 initially decided to account for the first and second order transverse derivatives. But in 2D, for example,
158 it amounts to cancel $\partial y', \partial x' y', \partial y'^2$ derivatives only and to achieve that, only three supplementary
159 cells are needed. Adding only three supplementary cells breaks the symmetry of the stencil, and such a
160 symmetry-breaking may render the preservation of the spectral resolution of the scheme more difficult.
161 Therefore, it was decided to account for all transverse derivatives up to the fourth order ($\partial y', \partial x' y',$
162 $\partial y'^2, \partial x'^2 y', \partial x' y'^2,$ and $\partial y'^3$) and to use four supplementary cells as Lacor et al. in 2D case (eight
163 supplementary cells in 3D). The list of all derivatives used are presented in Tab. 2. Fig. 4 presents the
164 resulting stencil in 2D case. The four points represented by a square are used to match the derivatives
165 in x' direction, and the four points represented by a circle (●) are used for transversal correction.

166 As it can be seen on Fig. 5, the two local frames (x', y') and (x'', y'') corresponding to the first and the
167 third local reference frames presented respectively, directly influence the transverse correction. In fact,
168 the four points (●) constitute a better stencil to approximate the derivative in the y'' direction than in
169 the y' one.

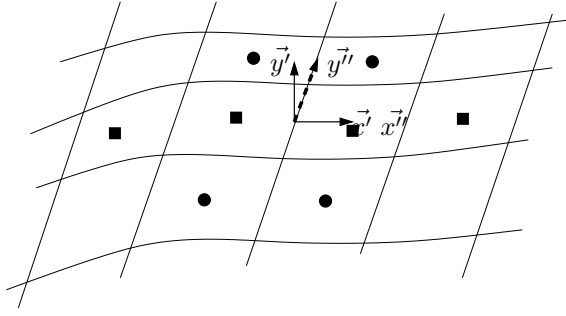


Figure 5: Local frame and discretization stencil

170 *2.2.3. Least-square error minimization*

171 However, at this point, in 2D for example, there are four supplementary coefficients than in the cartesian case and up to 6 supplementary relations to verify (see Tab. 2). So the final system is overdefined.
 172
 173 Those six relations (sixteen in 3D), are minimized by a least square approach but with a weighting distribution in order to give different importance to the contribution of the different transverse derivatives.
 174
 175 In particular, it has been numerically observed that the weighting coefficients relative to the first and second order derivatives must be larger than those relative to higher-order ones to get the best dissipation
 176
 177 and dispersion properties.

178 For sake of simplicity, the 2D case is considered. The interpolation equation reads :

$$\alpha \tilde{u}_{i-1/2,j} + \tilde{u}_{i+1/2,j} + \beta \tilde{u}_{i+3/2,j} = a \bar{u}_{i-1,j} + b \bar{u}_{i,j} + c \bar{u}_{i+1,j} + d \bar{u}_{i+2,j} + e \bar{u}_{i,j-1} + f \bar{u}_{i,j+1} + g \bar{u}_{i+1,j-1} + h \bar{u}_{i+1,j+1}. \quad (11)$$

179 The unknown coefficients are separated as $X = \left(\underbrace{\alpha, \beta, a, b, c, d}_{X_1}, \underbrace{e, f, g, h}_{X_2} \right)$. The final system obtained
 180 could be written

$$M.X = \left(\begin{array}{cc} A & B \\ A' & B' \end{array} \right) \left| \begin{array}{c} X_1 \\ X_2 \end{array} \right. = \left| \begin{array}{c} C \\ C' \end{array} \right. , \quad (12)$$

181 where A is a 6×6 matrix and B' a 6×4 matrix. $(A \ B)$ are the relations cancelling all derivatives in
 182 the principal direction, and $(A' \ B')$ are the relations cancelling all transverse derivatives. These matrix
 183 are normalized so that, the maximum coefficient of each line equals 1, *i.e.*

$$\max_j(M_{ij}) = 1, \forall i.$$

184 The part $(A \ B)$ of the system must mainly define X_1 , so it is not solved by the least square approach.
 185 Thus, the final system is

$$\left(\begin{array}{cc} I & 0 \\ 0 & \tilde{B}^T \end{array} \right) \left(\begin{array}{cc} A & B \\ A' & B' \end{array} \right) \left| \begin{array}{c} X_1 \\ X_2 \end{array} \right. = \left(\begin{array}{cc} I & 0 \\ 0 & \tilde{B}^T \end{array} \right) \left| \begin{array}{c} C \\ C' \end{array} \right. , \quad (13)$$

186 where, \tilde{B} is the matrix with rows defined as

$$L_i(\tilde{B}) = \omega_i L_i(B'). \quad (14)$$

187 ω_i is a weight defining how much better than other the transverse derivative corresponding to the row i
 188 must be cancelled.

189 2.3. Remarks

One can remark that for cartesian meshes, both approaches (the one using transverse derivatives and the one using the curvilinear abscissa) match (it is proved in appendix A).

The final compact formula is not directly applicable to boundaries of a closed domain. It is therefore necessary to set up a different scheme for boundaries and this is done in section 2.5.

To ensure that the tridiagonal matrix obtained with Eq. (8) is invertible, it is checked that it is diagonally dominant *i.e.*:

$$|\alpha| + |\beta| \leq 1,$$

190 otherwise, α and β are arbitrarily set to 1/3, thus the order is reduced to four. This generally happens
 191 when the mesh is strongly stretched or distorted. In this work, this situation happened, for example,
 192 when performing the linear convection on a 3D randomly perturbed mesh (see results presented in
 193 section 5.1.5).

194 2.4. Eigenvalues and spectral resolution

195 The spectral behavior of the proposed schemes is now analyzed considering the 1D linear convection
 196 equation :

$$\frac{\partial u}{\partial t} + \frac{\partial u}{\partial x} = 0. \quad (15)$$

197 The discretization of Eq. (15) by a FV method could be written in a FD-like matrix form:

$$\frac{d}{dt} \bar{U} = L \bar{U}, \quad (16)$$

198 where L is the space discretization operator and \bar{U} the vector of the cell-averaged values. The space
 199 discretization operator L is said to be stable if $\text{Re}(\lambda) \leq 0$, for any eigenvalue λ of L .

200 To study the spectral resolution of the scheme, an uniform 1D discretization of size h is considered,
 201 along with the following propagating wave solution:

$$u^k(x, t) = U^k e^{I(kx - \omega t)}. \quad (17)$$

202 One can show that, if the sixth-order compact interpolation is used on all points:

$$\bar{u}_i'^k = (L \bar{U})_i = I k' \bar{u}_i^k. \quad (18)$$

203 where k' is the modified wavenumber associated with the numerical scheme. Using the FD-like form
 204 of the scheme, one can find that k' is a real number and the scheme has the same spectral properties as
 205 the Lele's tridiagonal sixth-order compact scheme [14].

206 However, when a different scheme is applied on boundaries, the modified wavenumber differs on each
 207 point. To compute this local modified wavenumber, it is necessary to use the matrix form Eq. (16). One
 208 can write

$$\bar{U}'^k = L\bar{U}^k = IK'\bar{U}^k, \quad (19)$$

209 where K' is the diagonal matrix formed by the local modified wavenumber k'_i of each cell i . This local
 210 k'_i is very close to the one defined by Eq. (18) in the interior of the domain. On boundaries, k'_i is
 211 generally no longer real. The imaginary part introduces either a dissipative or an anti-diffusive effect.
 212 More precisely, a positive imaginary part corresponds to an anti-diffusion (amplification) since the wave
 213 propagate from the left to the right. Thus the study of this local modified wavenumber on boundaries
 214 as proposed by Sengupta et al. [22] gives a view of the spectral resolution and the local stability of the
 215 scheme at boundaries.

216 The next section presents some boundary closures at the interface boundary between two blocks.
 217 Firstly, a numerical study of eigenvalues of the space semi-discretization operator L gives a view of the
 218 global stability of the scheme. Then, a numerical study of local modified wavenumbers gives information
 219 about the spectral resolution and the local stability of the scheme at boundaries.

220 2.5. *Multiblock and periodic boundaries*

221 Since the aim of this work is to set up high order compact FV method for multiblock computations, a
 222 particular attention is paid to multiblock and periodic boundaries conditions. For these boundaries, two
 223 possibilities arise. The first possibility consists of keeping the interior scheme on boundaries. For periodic
 224 boundaries, one obtains a tridiagonal periodic matrix to solve. In case of multiblock multiprocessors
 225 computations, this option requires to solve the tridiagonal (even periodic) system in parallel, which may
 226 be very expensive. The second possibility is to use ghost cells and degenerate the scheme either by
 227 upwinding or by decreasing the order of accuracy. This is generally done by using a boundary scheme
 228 one order lower than the interior boundary scheme based on the works of Gustafsson [8], who shows that
 229 for hyperbolic problems, using explicit FD schemes, this insures the global scheme to keep the order of
 230 accuracy of the interior. But Kobayashi [12] shows, for Padé-like FV scheme, that the order of accuracy
 231 for the global scheme reduce to the one of the boundary closure. Therefore, decreasing the order of
 232 accuracy of the scheme could reduce the accuracy order on the whole domain. However, as important is
 233 to preserve high precision, another important constraint is to keep the conservativeness of the FV scheme
 234 and the stability.

235 In this work, only schemes using two ghost cells are investigated (see Fig. 6).

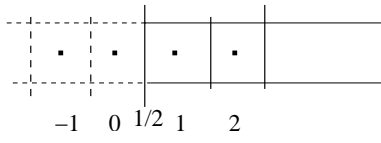


Figure 6: Ghost cells on the left boundary of the domain: cells indexed -1 and 0 are ghost cells, the interface 1/2 is the boundary interface of the domain.

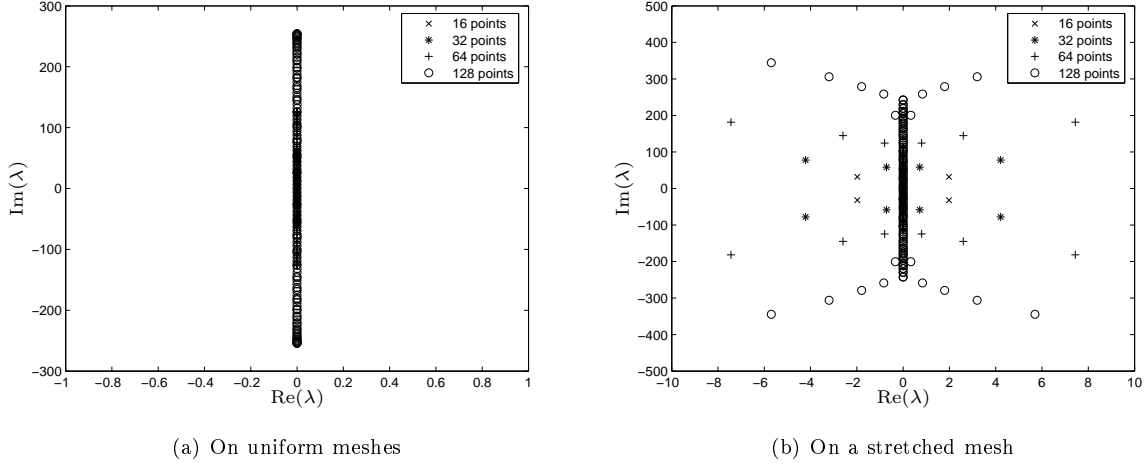


Figure 7: Eigenvalues spectra of the whole scheme using the Centered explicit boundary scheme (CEBC) on meshes of 16, 32, 64 and 128 points.

236 *2.5.1. Centered explicit boundary scheme (CEBC)*

237 The first scheme consists of using an explicit fourth-order interpolation on the first interface 1/2:

$$\tilde{u}_{1/2} = a\bar{u}_{-1} + b\bar{u}_0 + c\bar{u}_1 + d\bar{u}_2. \quad (20)$$

238 Then all other interfaces are computed with the usual sixth-order scheme. The stability analysis of the
 239 space discretization operator has shown that the scheme is stable on uniform meshes (see Fig. 7(a)).
 240 The spectral resolution has been studied for all frequencies on an uniform mesh with 40 cells. Fig. 8(a)
 241 shows that the scheme has good spectral resolution on the two first cells on each side of the domain
 242 but it presents possibility of anti-diffusion at the two last points of the domain for middle frequencies.
 243 However numerical tests have highlighted that the scheme become unstable on mesh with a stretching at
 244 the boundary even if the growth of the mesh size is only about 5% (see Fig. 7(b)). To fix these problems,
 245 two other possibilities have been explored.

246 *2.5.2. Upwind compact boundary scheme (UCBC)*

247 It is proposed to use a decentered fourth-order compact scheme at the boundary as:

$$\tilde{u}_{1/2} + \alpha\tilde{u}_{3/2} = a\bar{u}_{-1} + b\bar{u}_0 + c\bar{u}_1 + d\bar{u}_2. \quad (21)$$

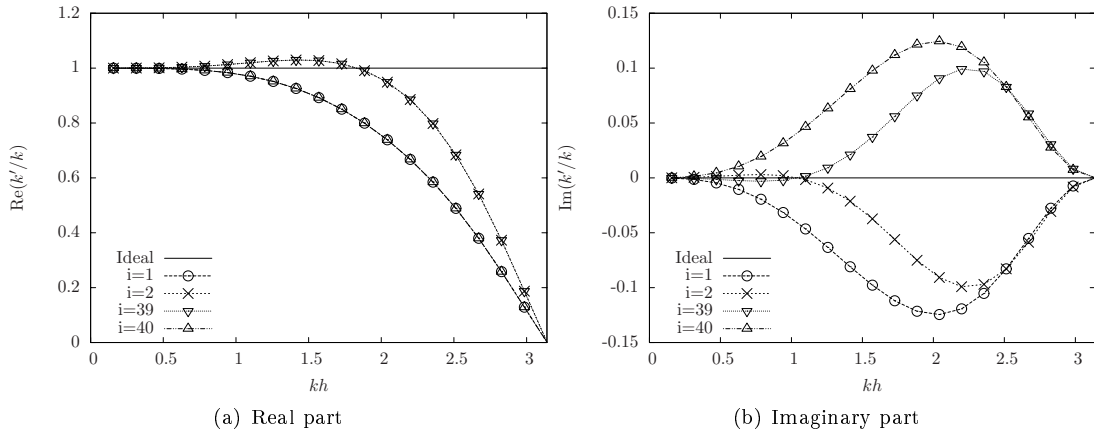


Figure 8: k'/k for the first derivatives in cells at boundaries using the Centered Explicit Boundary scheme (CEBC).

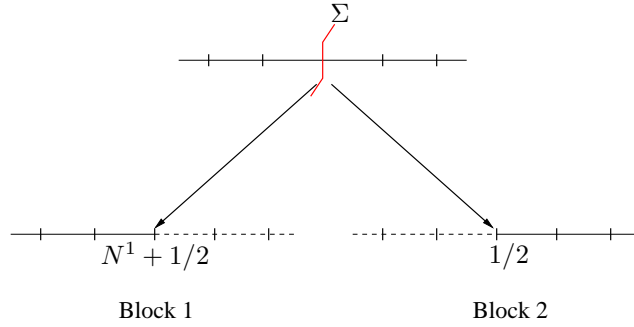


Figure 9: *Roe correction for a decentered scheme on a boundary.*

To obtain the scheme on the last interface, the stencil is just reversed.

The scheme is clearly non conservative, since the value at interface between two blocks is computed differently on the two blocks. This latter point is a disadvantage which could be corrected by applying a Riemann solver (e.g. Roe solver) with the two values computed on each block. For example let Σ be an interface between Block 1 and Block 2 as illustrated in Fig. 9. A left value $\tilde{u}_{N^1+1/2}^1$ on Σ is computed using the decentered compact scheme on Block 1, and the right value $\tilde{u}_{1/2}^2$ is computed on Block 2. Then, the flux on Σ is obtained thanks to the Roe solver:

$$F_{\Sigma} = F_{N^1+1/2}^1 = F_{1/2}^2 = F_{\text{Roe}}(\tilde{u}_{N^1+1/2}^1, \tilde{u}_{1/2}^2).$$

248 This Roe solver allows to account for the wave propagation direction. It does not correct anti-diffusion
 249 at near boundary cells (see Figs. 11(a),11(b)) but the eigenvalues study reveals that the scheme remains
 250 globally stable even on stretched meshes (see Figs. 10(a) and 10(b)) for $-1 \leq \alpha < 1$. Unfortunately, this
 251 approach is too expensive in parallel communications.

252 2.5.3. Decentered compact near boundary scheme (DCNBC)

253 This third approach aims to be a mix of the two previous methods. Here, the explicit fourth-order
 254 scheme is used on the first interface (1/2), while a decentered fifth-order compact scheme is employed

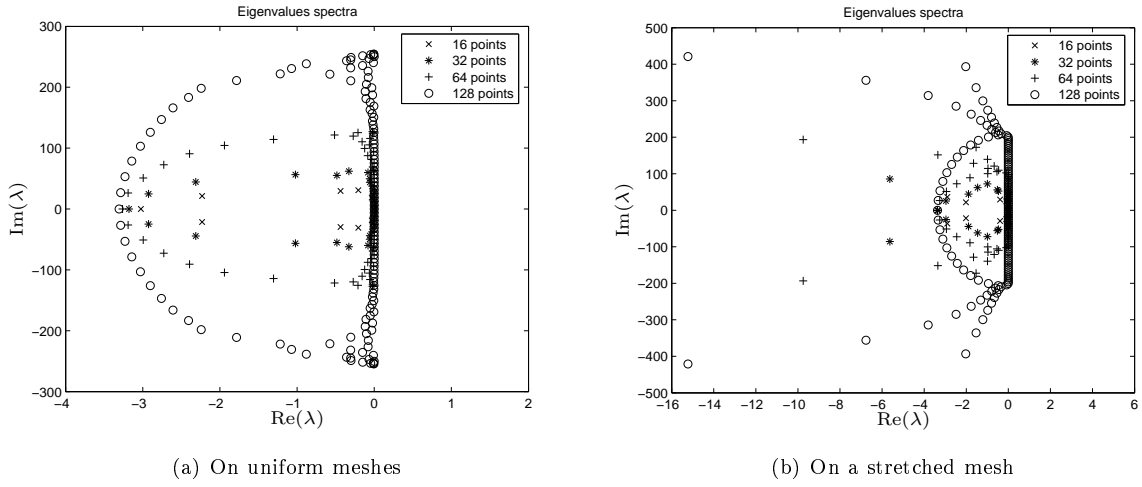


Figure 10: Eigenvalues spectra of the whole scheme using the UCBC ($\alpha = 2/3$) with a Roe solver boundary scheme on meshes of 16, 32, 64 and 128 points.

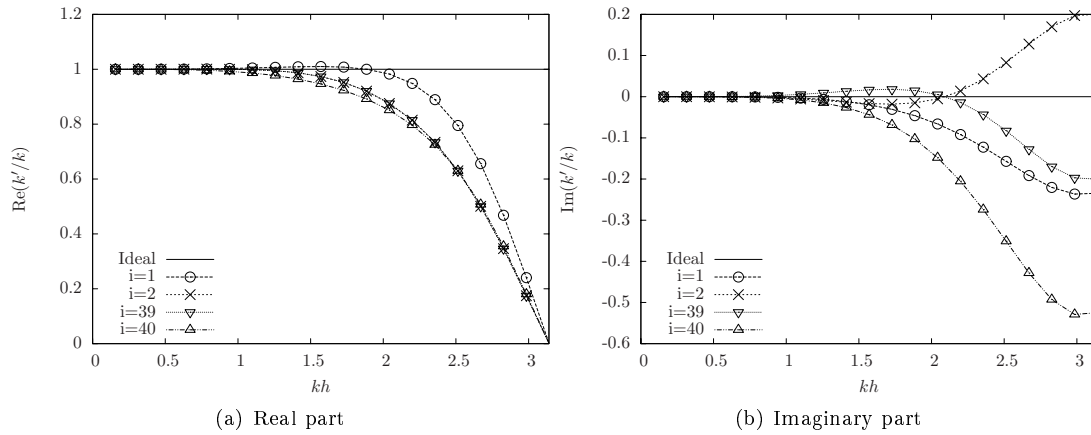


Figure 11: k'/k for the first derivatives in cells at boundaries using the UCBC ($\alpha = 2/3$) with a Roe solver boundary scheme.

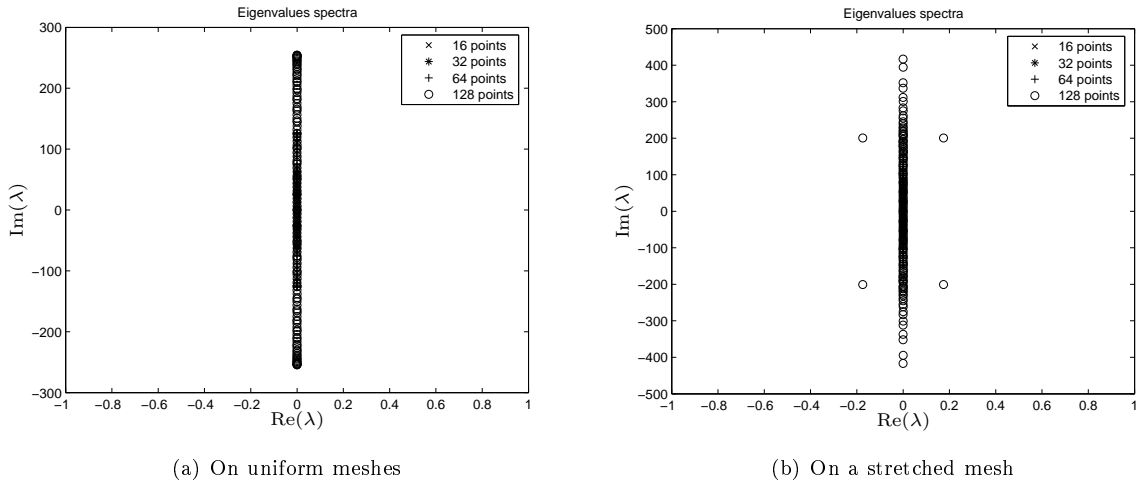


Figure 12: Eigenvalues spectra of the whole scheme using the DCNBC on meshes of 16, 32, 64 and 128 points.

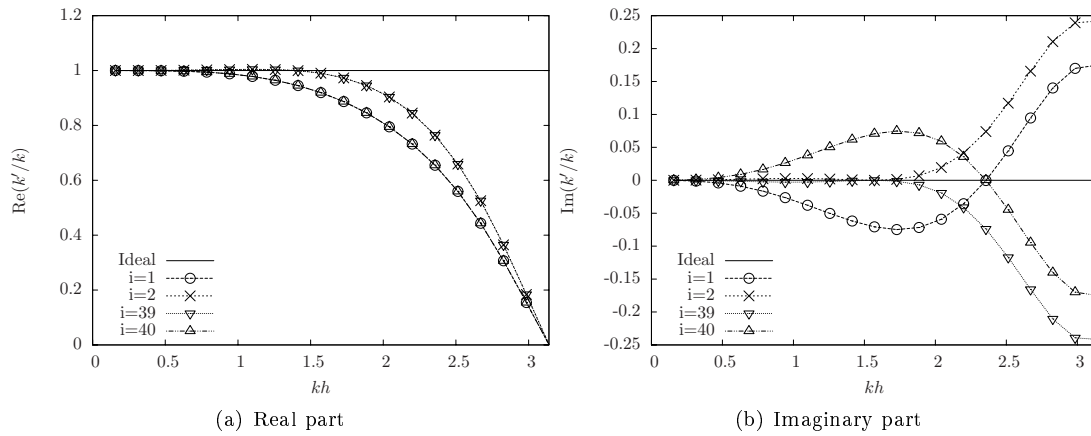


Figure 13: k'/k for the first derivatives in cells at boundaries using DCNBC.

255 on the second interface ($3/2$). To obtain a fifth-order scheme, only interior cells are used:

$$\alpha \tilde{u}_{1/2} + \tilde{u}_{3/2} + \beta \tilde{u}_{5/2} = \bar{b} \bar{u}_1 + \bar{c} \bar{u}_2 + \bar{d} \bar{u}_3. \quad (22)$$

256 This boundary closure is globally stable on uniform grids (see Fig. 12(a)). Although some eigenvalues have
 257 positive real part on stretched grids (Fig. 12(b)), numerical tests have shown that it is more stable than
 258 the CEBC. The whole scheme also presents possibility of anti-diffusion at middle and high frequencies
 259 on boundaries. Anti-diffusion at middle frequencies is less severe than on CEBC scheme. Anti-diffusion
 260 on high frequencies can be eliminated by filtering. Actually, filtering is generally needed to eliminate
 261 these high frequencies which are not solved by the scheme.

262 2.5.4. Summary

263 The three proposed boundary schemes have shown the same behaviour in terms of dispersion (real
 264 part of k'), which is present just at high frequencies; but for CUBC, this appears for higher frequencies

265 than for CEBC or DCNBC.

266 In terms of anti-diffusion, the CEBC scheme generates such phenomena even for middle frequencies while
 267 it is less severe for DCNBC and inexistant for CUBC. This amplification appears at higher frequencies
 268 for the two last schemes, especially for CUBC. However this behaviour is not so dramatic since special
 269 numerical treatment could be applied to damp these spurious waves. Even if CUBC seems to perform
 270 better, it will not be implemented in our solver for computational cost reasons.

271 3. Extension to non-linear cases

272 3.1. Discretization of the compressible Euler equations

273 Here are considered the compressible Euler equations written in conservative form:

$$\frac{\partial W}{\partial t} + \frac{\partial E}{\partial x} + \frac{\partial F}{\partial y} + \frac{\partial G}{\partial z} = 0, \quad (23)$$

274 where

$$W = (\rho, \rho u, \rho v, \rho w, \rho e)^t, \quad (24)$$

275 is the vector of conservative variables and

$$\begin{aligned} E &= (\rho u, \rho u^2 + p, \rho uv, \rho uw, (\rho e + p)u)^t, \\ F &= (\rho v, \rho uv, \rho v^2 + p, \rho vw, (\rho e + p)v)^t, \\ G &= (\rho w, \rho uw, \rho vw, \rho w^2 + p, (\rho e + p)w)^t \end{aligned}$$

276 are the convective flux densities.

277 The FV formulation requires to approximate the fluxes defined by

$$\tilde{\mathcal{F}}_{i+1/2,j,k} = \int_{S_{i+1/2,j,k}} (En_x + Fn_y + Gn_z) d\sigma, \quad (25)$$

278 on the interface $(i + 1/2, j, k)$. If assumed that the normal is constant along the interface, this leads to
 279 find an approximation of:

$$\tilde{\mathcal{F}}_{i+1/2,j,k} = S(\tilde{E}\tilde{n}_x + \tilde{F}\tilde{n}_y + \tilde{G}\tilde{n}_z), \quad (26)$$

280 where \tilde{E} , \tilde{F} and \tilde{G} are interface-averaged values of fluxes, and $(\tilde{n}_x, \tilde{n}_y, \tilde{n}_z)$ is the unitary normal of the
 281 interface.

282 To obtain a high-order compact FV scheme based on the compact interpolations presented in the previous
 283 sections, different approaches could be followed [17, 18, 13, 19] [17][18][13][19]. One of these approaches is
 284 to approximate \tilde{E} , \tilde{F} and \tilde{G} using interface-averaged values of conservative or primitive fields computed
 285 using the compact interpolation. However, when computing fluxes using interpolated mean values, a
 286 problem of precision arises. For instance, it is needed to compute the mean of the product ρuv , $\langle \rho u \rangle$, to
 287 approximate the flux. But approximating $\langle \rho u \rangle$ by $\langle \rho \rangle \langle u \rangle$ is a second order approximation. An idea is then

288 to compare the two values in order to determine which correction could be done to keep a higher order.
 289 Pereira et al. [17] shows that it is possible to make a correction to obtain a fourth-order approximation
 290 at a reasonable cost. This requires to approximate the first and second order derivatives respectively at
 291 the second and first order for ρ and u . This correction, extended by Lacor et al. [13] to arbitrary schemes
 292 notably improved the precision of his scheme on a rotation of a Gaussian wave test case. However,
 293 the correction was done assuming a Cartesian grid since for a general grid highly there is an important
 294 increase the cost of the computations. For sake of convenience, this approach and the others will be
 295 discussed in details in a next paper with more appropriate test cases since in the applications presented
 296 in the present paper, they do not make a valuable difference.

297 Therefore, for the vortex convection and acoustic scattering problems handled in the present paper,
 298 the following formulation (which is formally of the second order) is used, for each interface $(i + 1/2, j, k)$:

$$\tilde{\mathcal{F}} \approx S(E(\tilde{W})\tilde{n}_x + F(\tilde{W})\tilde{n}_y + G(\tilde{W})\tilde{n}_z). \quad (27)$$

299 where, \tilde{W} is the vector of the $(i + 1/2, j, k)$ interface-averaged values of the conservative variables.

300 3.2. Slip wall boundary condition treatment

301 In order to address some acoustic test cases, it is necessary to discuss the implementation of the
 302 slip wall boundary condition. This condition is treated as a symmetry condition. In the same way as
 303 multiblock and periodic boundary conditions it involves two layers of ghost cells whose metrics (points,
 304 normals, kinetic moments) and conservative fields are defined by symmetry. Indeed, let Σ on Fig. 14 be
 305 a symmetric boundary. Let M' be the symmetric of the point M with respect to Σ , following the normal
 306 \vec{n} . The symmetry condition induces:

$$\begin{cases} \rho(M') & = \rho(M), \\ \mathbf{u}(M') & = \mathbf{u}(M) - 2(\mathbf{u}(M) \cdot \mathbf{n})\mathbf{n}, \\ p(M') & = p(M). \end{cases} \quad (28)$$

307

308 It is then possible to use on this boundary either the CEBC or the DCNBC closures. For all test
 309 cases, the DCNBC closure has been applied.

310 4. Numerical stabilization

311 All spectral studies have shown that there is possibility of anti-diffusion of the scheme at high frequen-
 312 cies near boundaries. Thus, computations need to be stabilized. Filtering is a possible way to achieve
 313 it. The filters chosen are compact filters, precisely the sixth-order and eight-order filters proposed by
 314 Gaitonde and Visbal [4] have been used. The inner filter scheme reads:

$$\alpha_f \hat{u}_{i-1} + \hat{u}_i + \alpha_f \hat{u}_{i+1} = \sum_{n=-N}^N a_n \bar{u}_{i+n}, \quad (29)$$

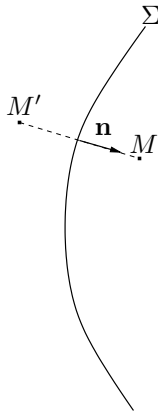


Figure 14: *Symmetric boundary condition.*

315 where α_f is a parameter ranging from $-1/2$ to $1/2$. The authors also recommend to use higher order one
 316 sided formulas on boundaries instead of decreasing the order of the filter. The one-sided formulas are
 317 defined by

$$\hat{u}_1 = \bar{u}_1, \quad (30)$$

$$\alpha_f \hat{u}_{i-1} + \hat{u}_i + \alpha_f \hat{u}_{i+1} = \sum_{n=1}^{2N+1} a_n \bar{u}_n, \quad i = 2, \dots, N. \quad (31)$$

318 The filtering is applied in the computational plane. In multidimensional case, filtering operator is applied
 319 successively in each dimension. One can remark that, in each direction, the first and the last points are
 320 not filtered. This could be a drawback since anti-diffusion is possible at this point. But for multiblock
 321 and periodic problems, it is possible to avoid it by using the two ghost cells values, so the first point non
 322 filtered is fictitious.

323 5. Applications

324 In this section, linear and non linear test cases are performed. The results of the proposed schemes
 325 are compared with two schemes using constant coefficients for the interface-averaged value interpolation.
 326 The first one (CEN4) is obtained using the explicit centered interpolation with constant coefficients,
 327 fourth-order on uniform grids, defined by

$$\tilde{u}_{i+1/2} = -\frac{1}{12}\bar{u}_{i-1} + \frac{7}{12}\bar{u}_i + \frac{7}{12}\bar{u}_{i+1} - \frac{1}{12}\bar{u}_{i+2}. \quad (32)$$

328 The second one (COMP46) is obtained using the compact interpolation with constant coefficients, sixth-
 329 order on uniform grids, defined by Eq. (9) for interior interfaces and the above explicit fourth-order
 330 centered interpolation Eq. 32 on the periodic boundary interfaces.

331 The first part of this section presents a model problem of linear convection on different types of grids.
 332 Then follows the presentation of some non linear applications.

334 In order to numerically assess the effective numerical properties of the schemes studied, a 2D linear
 335 convection problem is considered:

$$\frac{\partial \phi}{\partial t} + \mathbf{v} \cdot \nabla \phi = 0. \quad (33)$$

An initial Gaussian wave

$$\phi(x, y) = 1 + 0.25 \exp(-38.(x^2 + y^2)),$$

336 is convected through a computational domain comprised in the square region $-1 \leq x, y \leq 1$ at the speed
 337 $\mathbf{v} = (1, 1)$. Periodic boundary conditions are applied on all boundaries. The convection following this
 338 diagonal direction makes the test case really sensitive to boundary closures and breaks the preferred
 339 direction which could exist in the used grids.

340 The time integration scheme used for these computations is the following four steps Runge-Kutta
 341 method [11]

$$\begin{cases} u^{(0)} &= u_n, \\ u^{(k)} &= u^{(0)} + \alpha_k \Delta t L(u^{(k-1)}), \quad k = 1, \dots, 4, \\ u_{n+1} &= u^{(4)}, \end{cases} \quad (34)$$

with L , the space discretization operator and

$$\alpha_1 = \frac{1}{4}, \alpha_2 = \frac{1}{3}, \alpha_3 = \frac{1}{2}, \alpha_4 = 1.$$

342 This scheme is fourth-order accurate for linear problems.

343 In summary, four numerical schemes have been numerically studied:

- 344 1. CART46 which uses the cartesian-like sixth-order compact scheme using curvilinear abscissa for
 345 the interior interfaces and the CEBC closure scheme;
- 346 2. CART456 which differs from the previous in that it uses the DCNBC closure scheme;
- 347 3. CUR46 which is the general FV curvilinear scheme using the CEBC closure scheme;
- 348 4. CUR456 which is the general FV curvilinear scheme using the DCNBC closure scheme.

349 It is worth reminding that on cartesian uniform grids, the CART46, CUR46 and COMP46 schemes are
 350 the same. On another hand, the CART456 and the CUR456 schemes are the same.

351 Concerning the CURxxx methods, two types of parameters are to be specified: the local reference frame
 352 and the weights used for the least square method. The codes (ORTH, NORM and GEN) of the local
 353 reference frames used are shown in Tab. 3. The combinations of weights (W1, W2 and W3) used described
 354 in Tab. 4. When it is not specified, the local reference frame ORTH and the weights combination W2 is
 355 used.

356 The different schemes are often coupled with the filter operator. When it is the case, it is mentioned in
 357 the title of the scheme using the letter F followed by the order of the filter and the coefficient of the filter
 358 (e.g.: F80.49 for the eight-order filter with $\alpha_f = 0.49$). The filter is applied after the last Runge-Kutta
 359 step.

Code	Local reference frame
ORTH	Orthonormal local reference frame with the x' direction defined by the direction between the adjacent cells centers (Fig. 3(a))
NORM	Orthonormal local reference frame with the x' direction defined by the normal of the face (Fig. 3(b))
GEN	Non-orthogonal local reference frame with the direction defined by the neighbouring cells centers (Fig. 3(c))

Table 3: Codes of the local reference frames used for the CURxxx methods

Derivatives	Weights W1	Weights W2	Weights W3
1 st order: $\partial y', \partial z'$	1	100	500
2 nd order: $\partial^2 x' y', \partial^2 y'^2, \partial^2 x' z', \dots$	1	100	500
3 rd order: $\partial^3 x' y'^2, \partial^3 x' z'^2, \partial^3 x'^2 y', \dots$	1	1	1

Table 4: Weights used in general for the least square method applied on transverse derivatives relations: the z' derivatives are not considered in 2D cases.

360 Different meshes are used in order to highlight different properties of the proposed schemes. Therefore,
361 to retrieve the numerical order of the schemes, only meshes which can be refined or coarsened using the
362 same initial property of the mesh are used: uniform cartesian and wavy meshes. All meshes help to assess
363 the stability, the dissipation and dispersion properties of the schemes. Stretched cartesian grid and non
364 uniform cartesian grid consisting in alternating bigger and smaller cells help to assess the importance of
365 taking into account non-uniformity on cartesian grid. On another hand, wavy grids and highly irregular
366 grid obtained by randomly perturbing an uniform cartesian grid highlight the importance of taking into
367 account shape, size and direction variations in curvilinear grids.

368 Hence, seven types of grids have been used (see Figs. 15 and 16):

- 369 • UNIF: uniform cartesian grid;
- 370 • STRETCH: a stretched cartesian grid with a maximum stretch ratio of 1.05;
- 371 • ALT: a cartesian grid consisting in alternating bigger and smaller cells with a size ratio of 11/9;
- 372 • WAVY I: an uniform wavy grid defined by

$$\begin{cases} x_{ij} &= x_{\min} + \Delta x \left[(i-1) + A_x \sin \left(\frac{n_x \pi (j-1) \Delta y}{L_y} \right) \right] \\ y_{ij} &= y_{\min} + \Delta y \left[(j-1) + A_y \sin \left(\frac{n_y \pi (i-1) \Delta x}{L_x} \right) \right] \end{cases}, \quad (35)$$

with

$$1 \leq i, j \leq N$$

$$\Delta x = \frac{L_x}{N-1}, \quad \Delta y = \frac{L_y}{N-1},$$

373 where N denotes the number of points in the x and y directions, $L_x = x_{\max} - x_{\min}$ and $L_y =$
374 $y_{\max} - y_{\min}$ are the lengths of the domain in the x and y directions respectively. $n_x = n_y = 8$ and
375 $A_x = A_y = 2/r$ where r is fixed such that $rN = 128$. This parameter r allows to obtain a mesh
376 which is a coarsen mesh of the mesh obtained with $N = 128$ and $r = 1$.

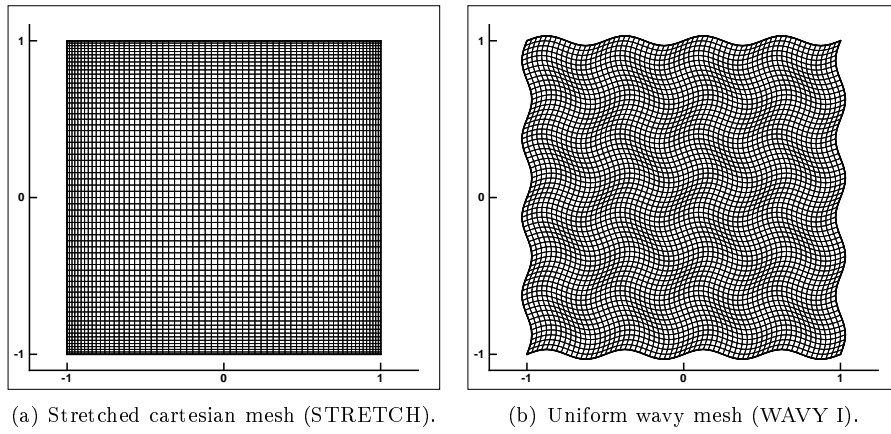


Figure 15: 64×64 -cells Meshes used for computations.

- WAVY II: a highly distorted uniform wavy grid defined by

$$\begin{cases} x_{ij} = \bar{x}_{ij} + 0.02L_x \sin(2\pi \frac{(\bar{y}_{ij}-y_0)}{L_y}) \\ y_{ij} = \bar{y}_{ij} + 0.04L_y \sin(16\pi \frac{(\bar{x}_{ij}-x_0)}{L_x}) \end{cases}, \quad (36)$$

where $(\bar{x}_{ij}, \bar{y}_{ij})$ are the coordinates of the cartesian uniform mesh of the same size, L_x and L_y , the lengths of the domain in the x and y directions respectively, and (x_0, y_0) , the center of the domain.

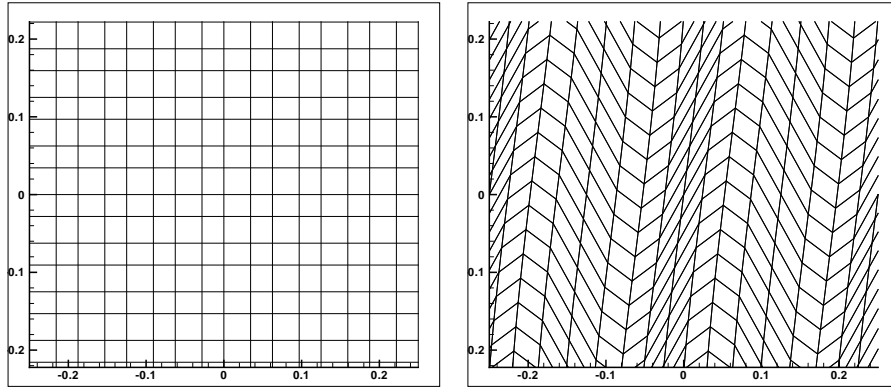
- WAVY III: a highly distorted wavy grid obtained from the ALT grid of the same size using Eq. (36);
- RAND: a highly irregular grid obtained by randomly perturbing an uniform grid with a maximum amplitude of 20%.

5.1.1. Effective order of accuracy

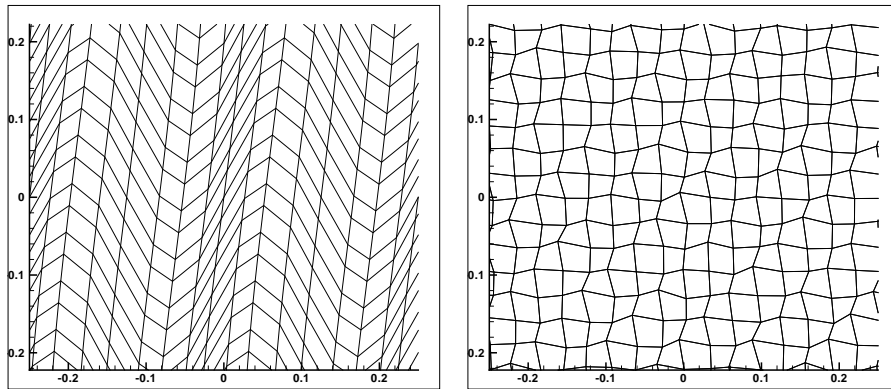
To measure the numerical order of accuracy of the different schemes, the three types of grids used are the UNIF, WAVY I and WAVY II grids. For the first two types, four different grid resolutions have been considered to retrieve the effective order of accuracy: 16×16 , 32×32 , 64×64 and 128×128 . For the WAVY II grids, a 256×256 grid is also used since the 16×16 grid is so coarse that the domain defined by WAVY II grids is not completely described.

The time step is chosen very small so that the time integration error could be neglected in comparison to the spatial one. The error between the computed solution after one period (*i.e.*, the time for the wave to return to the initial position for the first time) and the initial solution is found using the L_2 -norm. Fig. 17 displays the evolution of the error versus the mesh size and Tab. 5, Tab. 6 and Tab. 7 give the observed order of accuracy obtained on the uniform cartesian and wavy grids. For sake of clarity, for WAVY I and WAVY II grids, only the errors for CART46, CUR46 and COMP46 schemes are plotted on graphs.

On the more distorted wavy mesh (WAVY II), CARTxxx and CURxxx methods need to be stabilized with filtering. And when filtered, the errors obtained are almost the same for CART46 and CART456



(a) Cartesian grid alternating bigger and smaller cells with the size ration 11/9 (ALT). (b) Highly distorted wavy mesh obtained from the UNIF grid (WAVY II).



(c) Highly distorted wavy mesh obtained from the ALT grid (WAVY III). (d) Perturbed mesh obtained by randomly perturbing the UNIF grid (RAND).

Figure 16: 64×64 -cells ALT, WAVYII, WAVY III and RAND meshes magnified.

Mesh size	CART46		CART456	
	Error	Order	Error	Order
16×16	2.52×10^{-4}	-	1.88×10^{-4}	-
32×32	7.55×10^{-6}	5.06	5.31×10^{-6}	5.14
64×64	1.02×10^{-7}	6.20	6.36×10^{-8}	6.38
128×128	1.67×10^{-9}	5.93	9.16×10^{-10}	6.11

Table 5: Numerical mean errors and orders of schemes on uniform cartesian meshes (UNIF) for the 2D linear convection.

Mesh size	CART46		CUR46		COMP46	
	Error	Order	Error	Order	Error	Order
16×16	5.13×10^{-4}	-	4.01×10^{-4}	-	5.13×10^{-4}	-
32×32	1.03×10^{-5}	5.63	1.05×10^{-5}	5.25	1.23×10^{-5}	5.38
64×64	1.44×10^{-7}	6.16	1.57×10^{-7}	6.06	1.91×10^{-7}	6.00
128×128	2.34×10^{-9}	5.94	3.36×10^{-9}	5.54	3.18×10^{-9}	5.9

Mesh size	CART456		CUR456	
	Error	Order	Error	Order
16×16	5.33×10^{-4}	-	3.91×10^{-4}	-
32×32	7.56×10^{-6}	6.13	7.72×10^{-6}	5.66
64×64	8.68×10^{-8}	6.44	1.00×10^{-7}	6.27
128×128	1.31×10^{-9}	6.05	2.85×10^{-9}	5.13

Table 6: Numerical mean errors and orders of schemes on uniform wavy meshes (WAVY I) for the 2D linear convection.

398 schemes and for CUR46 and CUR456 schemes. It is noteworthy that the NORM frame is used since
399 it was impossible to stabilize computations using the ORTH frame for this WAVY II mesh. This is
400 explained further when dealing with long-time convection simulations.

401 One can see that the averaged order of accuracy of the different methods for UNIF and WAVY I grids is
402 higher than 5. The results for the WAVY II grids are more difficult to explain. In fact, the order retrieved
403 when passing from the 16×16 grid to the 32×32 grid is less than one. The reason has already been
404 mentioned: the 16×16 grid is too coarsen and discretizes a domain too different from the one defined
405 by other WAVY II grids. This grid is almost uniform but with slight deformations in the y direction so
406 the COMP46 method performed very well while the other methods introduces some errors because the
407 filtering was used. When passing from the 128×128 grid to the 256×256 grid, the usage of the scheme
408 in physical space probably allows to cancel out more higher-order terms than formally predicted than
409 the COMP46 method.

410 5.1.2. Stability, dissipation and dispersion properties on uniform grids

411 To analyze the stability, the dispersion and dissipation of the different schemes, computations have
412 been carried out for 25 periods on the 64×64 grids. This section presents the results obtained on uniform
413 grids UNIF, WAVY I and WAVY II. It is shown that the proposed schemes behave well on uniform grids.
414 The results obtained on the WAVY II grid highlight the importance of the local reference frame for the
415 CURxxx methods.

416 Results of the simulation on the uniform grid are shown in Fig. 18. The CEN4 scheme is obviously
417 the most dispersive one since many local extrema are generated. The proposed schemes behaves very

Mesh size	CART46F80.49		CUR46F80.49-NORM		COMP46	
	Error	Order	Error	Order	Error	Order
16×16	1.84×10^{-4}	-	1.84×10^{-4}	-	1.04×10^{-4}	-
32×32	6.23×10^{-5}	1.56	6.22×10^{-5}	1.56	7.35×10^{-5}	0.50
64×64	4.0×10^{-6}	3.96	4.01×10^{-6}	3.95	4.08×10^{-6}	4.17
128×128	3.03×10^{-8}	7.04	2.91×10^{-8}	7.10	3.14×10^{-8}	7.02
256×256	1.46×10^{-10}	7.69	4.12×10^{-11}	9.46	5.29×10^{-10}	5.89

Mesh size	CART456F80.49		CUR456F80.49-NORM	
	Error	Order	Error	Order
16×16	1.84×10^{-4}	-	1.84×10^{-4}	-
32×32	6.23×10^{-5}	1.56	6.22×10^{-5}	1.56
64×64	4.01×10^{-6}	3.95	4.02×10^{-6}	3.95
128×128	3.04×10^{-8}	7.04	2.94×10^{-8}	7.09
256×256	1.47×10^{-10}	7.68	4.87×10^{-11}	9.23

Table 7: Numerical mean errors and orders of schemes on highly distorted wavy meshes (WAVY II) for the 2D linear convection.

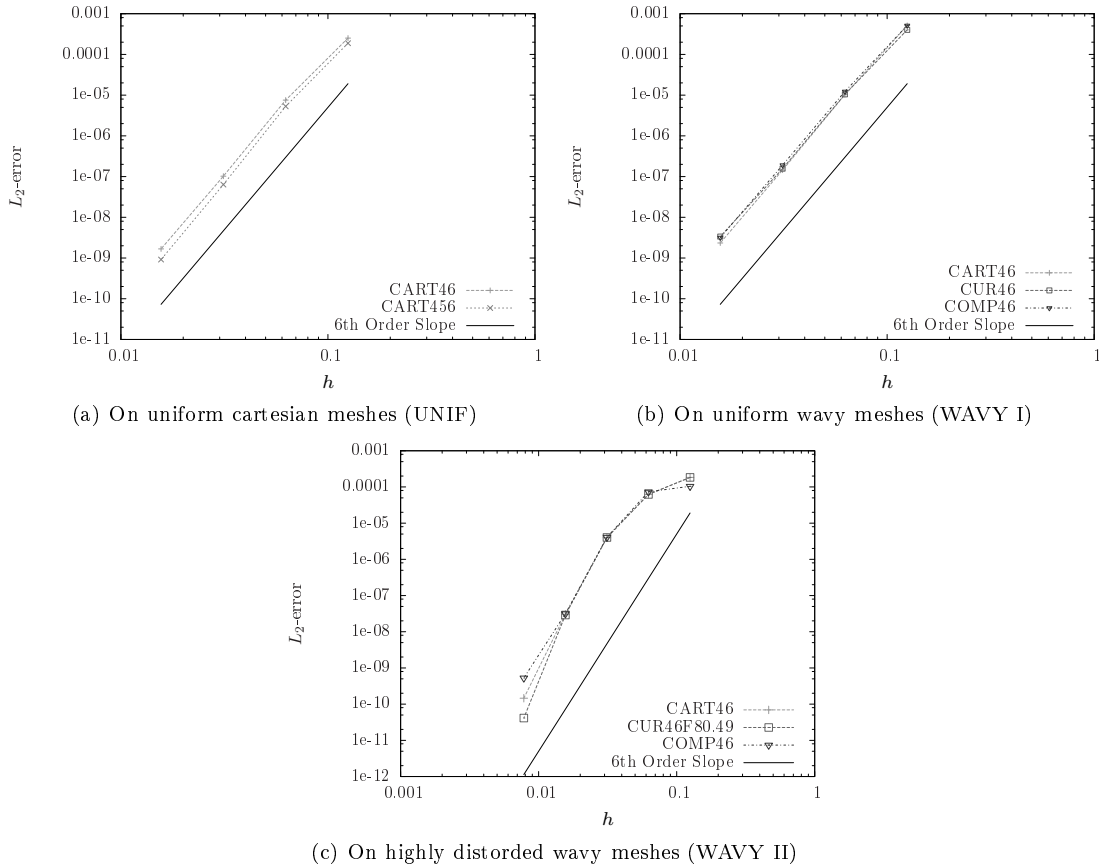


Figure 17: Evolution of the errors following the mesh size for the 2D linear convection.

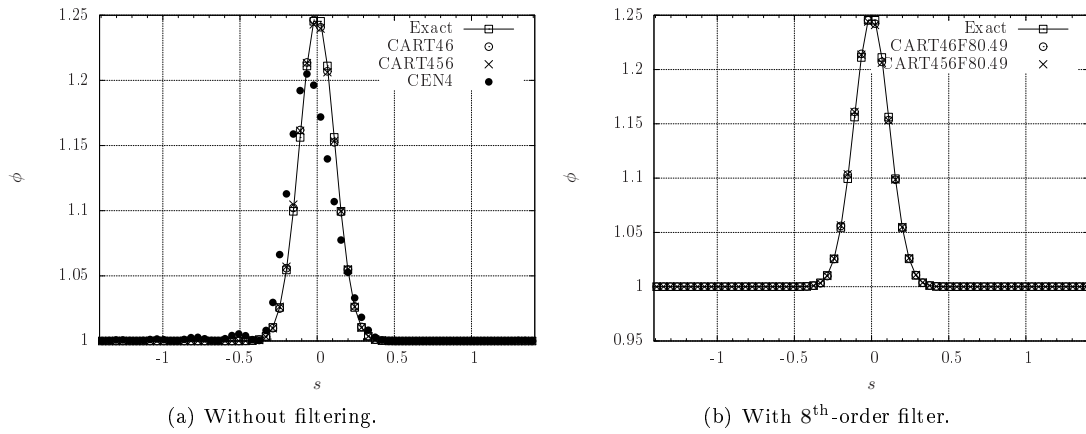


Figure 18: Profiles along the line $x = y$ of a linear convection equation solution on the uniform cartesian mesh (UNIF) after 25 periods.

418 well. The eight-order filter does not deteriorate the results obtained.

419 Fig. 19 shows results obtained on the WAVY I mesh after 25 periods. In this case, COMP46 method
 420 is stable and gives good results. It shows that a computational space formulation is stable and efficient
 421 on smooth grids even curvilinear. The CART46 and CUR46 methods seems to be the most stable of the
 422 proposed schemes since all others need filtering. This shows the limitations of a 1D approach as it has
 423 been done in the eigenvalues and spectral study of section 2.5 to analyze the stability of a scheme on
 424 curvilinear grids. Until now, no explanation has been found to justify this phenomenon. However when
 425 filtering is applied all the methods give similar results.

426 It is worth noting that the eighth-order filter with one-sided formulas failed to stabilize CART456 and
 427 CUR456 schemes. But the cyclic eight-order filter (not using eight-order one-sided formulas on bound-
 428 aries), which is used for the results shown, stabilizes the computations. This problem could come either
 429 from the one-sided formulations on boundaries either from the fact that the first point is not filtered.
 430 Results obtained on the vortex convection and presented further show that the latter fact is probably
 431 the main reason. Therefore, it is inadequate to leave the first cell of the domain unfiltered as it is done
 432 with one-sided filter on boundaries.

433 Since, on wavy meshes, filtered CARTxxx methods behave similarly, as well as CURxxx, computations
 434 results on the highly distorted mesh (WAVY II) are shown only for schemes using the CEBC boundary
 435 closure. For this WAVY II mesh, all the methods (even the CEN4 method) are unstable except the
 436 COMP46 one. However its results (not shown) are pretty dispersive. To compare them with equal
 437 parameters, the filter has been applied to all methods. In Fig. 20(a), one can observe that on highly
 438 distorted meshes, the filtered CARTxxx method are finally more dispersive and more dissipative than
 439 the scheme using constant coefficients (COMP46) and filtering. One can conclude that it is not sufficient
 440 to use the curvilinear abscissa when mesh line directions vary strongly. This is confirmed by results
 441 obtained further on non-uniform curvilinear meshes. The filtered COMP46 method is slightly more
 442 dissipative than the filtered CURxxx methods.

443 It is worth noting that the CUR46 method used has been computed using the GEN frame. In Fig. 20(b),

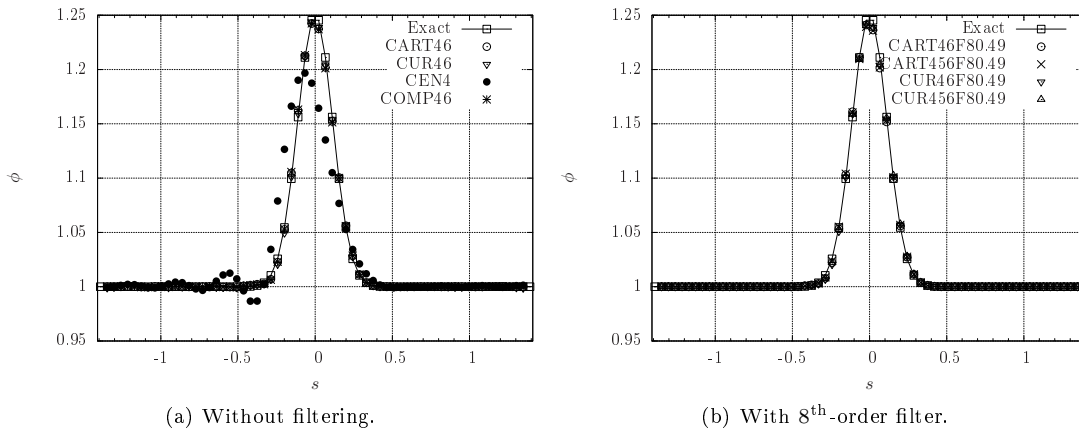


Figure 19: Profiles along the line $x = y$ of a linear convection equation solution on the uniform wavy mesh (WAVY I) after 25 periods.

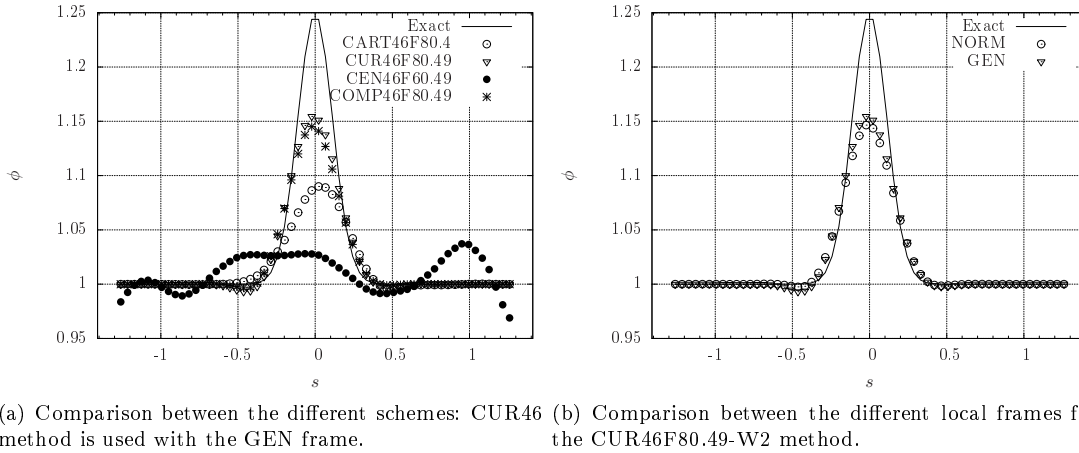


Figure 20: Profiles along the line $x = y$ of a linear convection equation solution on the distorted wavy mesh (WAVY II) after 25 periods.

444 a comparison is made between the results obtained with this latter method and those obtained using the
 445 orthogonal local frame defined by the interfaces normals. Results are pretty similar, however it could
 446 be observed that the results with GEN frame are better in terms of dissipation while the NORM ones
 447 present a slightly better behaviour in terms of dispersion. The computations using the ORTH frame
 448 lead to an non diagonally dominant matrix to inverse. For these test cases, the restriction to the fourth-
 449 order has not been done so the computations are unstable even with the filtering. But this allows to
 450 conclude that the local frame plays an effective role (although not sufficient) on the stability and on the
 451 dispersion-dissipative effects of the solution. Something noteworthy is the fact that the transverse axe is
 452 pretty the same for the NORM and GEN frames. It could indicate that the good discretization of the
 453 transverse derivatives in the two frames (as explained in section 2.2.2) is the reason of the better results
 454 obtained. Indeed, this discretization is less good for the CURxxx method with ORTH frame and absent
 455 for the CARTxxx methods. On meshes with very strongly varying grid lines directions, the GEN frame
 456 is the best to get the lowest dissipation effect.

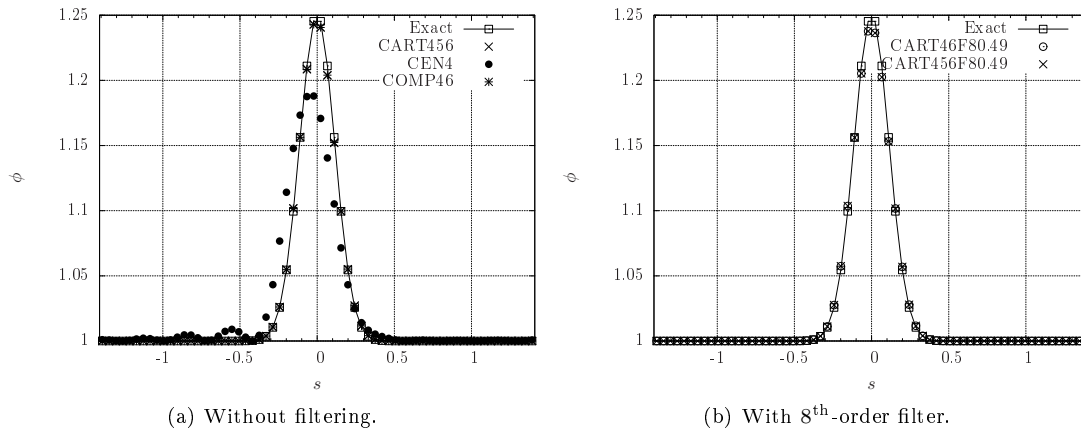


Figure 21: Profiles along the line $x = y$ of a linear convection equation solution on the stretched cartesian mesh (STRETCH) after 25 periods.

457 5.1.3. Stability, dissipation and dispersion properties on non-uniform cartesian grids

458 This section presents computations done for 25 periods on 64×64 non-uniform cartesian grids
 459 STRETCH and ALT. The results obtained on both grids confirms the conclusion of the eigenvalues
 460 study of the multiblock boundary closures. Meanwhile the results obtained on the ALT grid highlight
 461 the necessity to take into account the non-uniformity of cartesian grids.

462 Fig. 21 shows results on the stretched mesh after 25 periods. The CART46 method is not stable
 463 without filtering whereas the CART456 yields very satisfactory results. Hence, this confirms that on this
 464 type of grids, CEBC boundary closure is really less stable than DCNBC boundary closure as foreseen by
 465 the eigenvalues study. However, the COMP46 method is stable without filtering. This is easily explained
 466 by the fact that, when processing interfaces on the same mesh line, the COMP46 scheme behaves like
 467 if the mesh was uniform. Moreover, since the interfaces on this mesh line have the same normal, when
 468 computing the fluxes balances in the mesh line direction, these fluxes balances behave like the 1D space
 469 discretization operator on an uniform grid. Therefore the scheme is stable as it is on uniform grids.
 470 Taking into account the non-uniformity breaks this stability property for the CART46 scheme.

471

472 According to those previous results, it seems like taking into account non-uniformity of the grid is
 473 not necessary. Results obtained on the ALT scheme shows that it is certainly not the case. Fig. 22
 474 shows results obtained using the different schemes. Although the COMP46 scheme is stable, it is very
 475 dispersive and pretty anti-diffusive. It is therefore possible that the scheme becomes unstable for longer
 476 simulations. This is a real drawback since the alternating size ratio is not so important. Once again, the
 477 CART46 scheme is not stable while the CART456 one is. The use of the filter does not completely solve
 478 the problem. Something interesting to see here is the fact that using the filter introduces little dispersion
 479 to the CART456 results, even when using a cyclic formulation. It can indicate that the filter could be
 480 also a source of dispersion effects when dealing with non-uniform grids. However, it is clear that taking
 481 into account non-uniformity of grids is important.

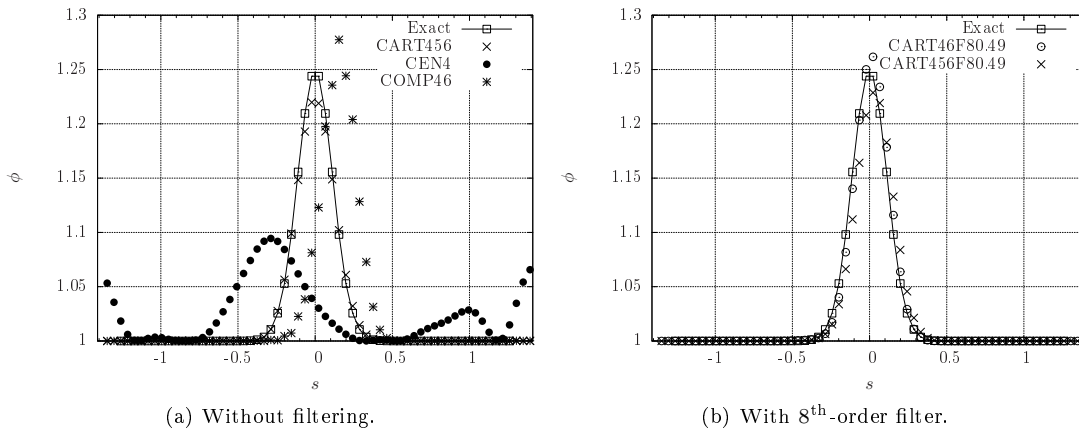


Figure 22: Profiles along the line $x = y$ of a linear convection equation solution on the mesh alternating bigger and smaller cells with a size ratio of 11/9 (ALT) after 25 periods.

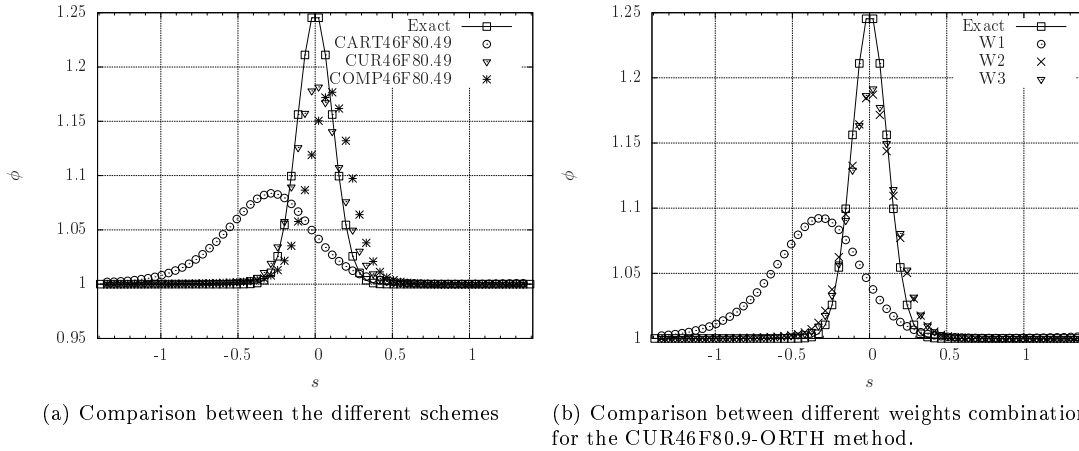


Figure 23: Profiles along the line $x = y$ of a linear convection equation solution on the RAND mesh after 25 periods.

482 5.1.4. Stability, dissipation and dispersion properties on non-uniform curvilinear meshes

483 This section deals with non-uniform curvilinear meshes: RAND and WAVY III. A first interesting
 484 conclusion is that, when dealing with non-uniform curvilinear meshes, it is not sufficient and even not
 485 recommended to use a scheme using only the curvilinear abscissa. However, it is clearly shown that
 486 taking into account shape, size and mesh lines directions variations is important to get lowest dissipation
 487 and dispersion effects. Computations done on RAND grid highlight the importance of weights used for
 488 the least square method.

489 The results obtained on the RAND mesh are presented in Fig. 23(a)). All schemes are unstable
 490 without filtering. Using filtering, CURxxx schemes are obviously superior to CARTxxx and COMP46
 491 schemes in terms of dissipation and dispersion. Dissipation effects are extremely important for CARTxxx
 492 schemes. It is possible that those schemes develop strong high frequencies waves which are damped by
 493 the filter.

494 It is important to note that in the weighted least square method, the weight of the first order and
 495 second order transverse derivatives has to be more important than the higher order transverse derivatives

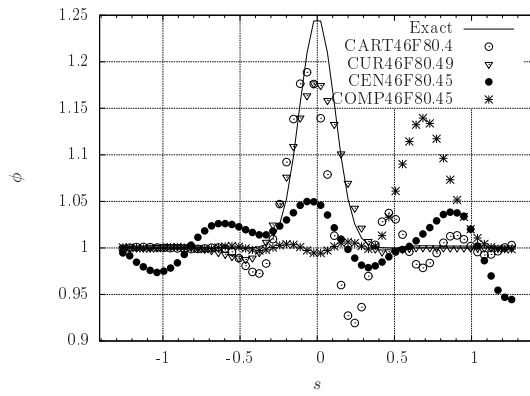


Figure 24: Profiles along the line $x = y$ of a linear convection equation solution on the WAVY III mesh after 25 periods: the CUR46 method uses the NORM frame.

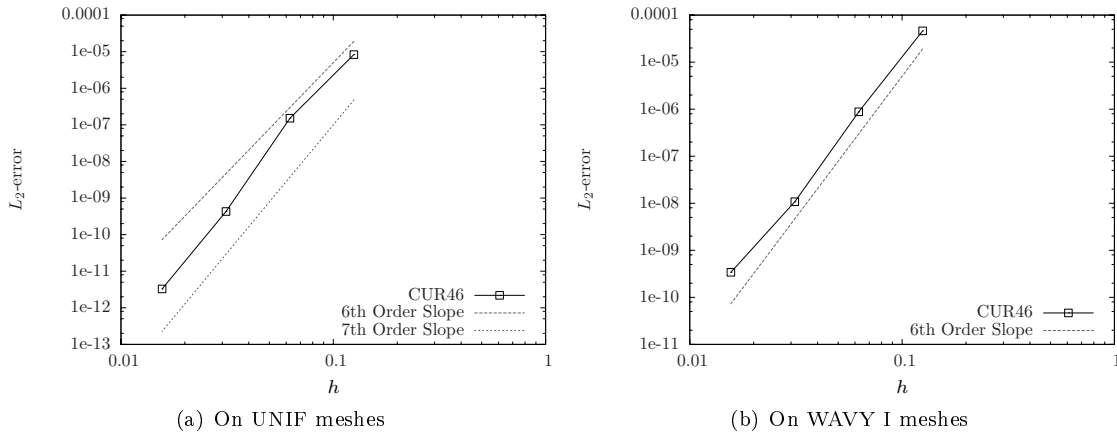


Figure 25: Evolution of the errors following the mesh size for the 3D linear convection: the GEN Frame and the W2 weights extended to 3D have been used.

506 according to results presented in Fig. 23(b). Otherwise CURxxx schemes behave like CARTxxx schemes.
 507 The results in Fig. 23(b) also show that the weight combination W2 chosen for all simulations is sufficient
 508 to get the best possible results.

509 Fig. 24 shows results obtained on the WAVY III meshes. None scheme is stable without filtering.
 500 Once again, it is clear that CURxxx methods show a better behaviour than all other schemes. Other
 501 methods introduce an important dispersion effect which completely denaturates the solution. Thus, the
 502 CURxxx methods, which account for the variation of the cells shapes and sizes and of the mesh lines
 503 directions, are more capable to handle non-uniform curvilinear meshes.

504 5.1.5. 3D Computations

505 To show the capability of the CURxxx schemes to treat three dimensional flows, a rapid study of
 506 the numerical accuracy order and of the stability, dissipation and dispersion properties of the CURxxx
 507 scheme have been performed. The same numerical order has been retrieved as it can be seen in Fig. 25.

508 A long-time convection simulation has been performed but for a larger convection time (50 periods)
 509 on a $64 \times 64 \times 64$ RAND mesh. The GEN frame and the W2 weights combination are used. It is
 510 noteworthy that, for a limited number of points, the tridiagonal system obtained was not diagonally

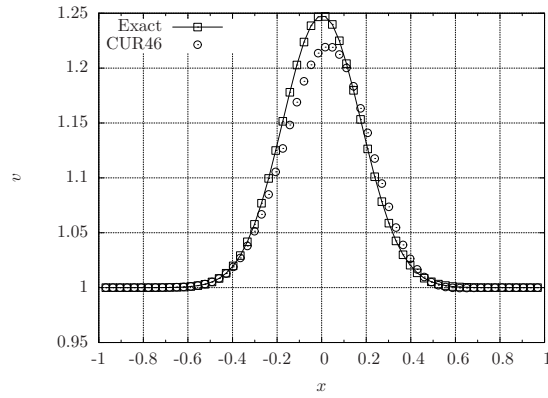


Figure 26: $y = 0$ profile of a linear convection equation solution on a 3D RAND mesh after 50 periods: the GEN Frame and the W2 weights extended to 3D have been used..

511 dominant. In this case, the restriction to the fourth-order by fixing $\alpha = \beta = 1/3$ has been activated.
 512 However, the good behavior of the CURxxx appears clearly in Fig. 26.

513 5.1.6. Conclusion on linear computations

514 These numerical tests have shown that the proposed schemes have good accuracy and spectral res-
 515 olution on regular curvilinear meshes although the more general FV schemes (CURxxx) need to be
 516 stabilized for long computations. However, if all methods give pretty similar results on regular meshes,
 517 CURxxx schemes are more accurate, low dissipative and low dispersive than the cartesian like schemes
 518 (CARTxxx) and than the schemes using constant coefficients (COMP46) when dealing with irregular
 519 curvilinear meshes.

520 The next sections aim to validate the different schemes with the approach defined by Eq. (27) in a
 521 non linear context and on problems requiring high precision and spectral resolution, some applications
 522 have been performed with the code `elsA` of ONERA for aerodynamics simulations [2]. Two test cases
 523 have been selected:

- 524 • the convection of a vortex on a 2D square region with periodic boundary conditions in all directions;
- 525 • the scattering of an acoustic wave diffracted by a plane wall boundary;

526 All these cases are realized using the following third order three steps TVD Runge-Kutta algorithm of
 527 Gottlieb and Chi-Shu [7]:

$$\begin{cases} u^{(0)} &= u_n, \\ u^{(k)} &= (1 - \alpha_k)u^{(0)} + \alpha_k u^{(k-1)} + \alpha_k \Delta t L(u^{(k-1)}), \quad k = 1, \dots, 3, \\ u_{n+1} &= u^{(3)}, \end{cases} \quad (37)$$

with

$$\alpha_1 = 1, \alpha_2 = \frac{1}{4}, \alpha_3 = \frac{2}{3}.$$

528 Filters have been implemented using one-sided boundaries formulas. However, filters are applied on
 529 fictitious cells also so that the unfiltered points are the fictitious cells. So the first points of the domain are

530 filtered and computations are better stabilized. Because of programming constraints, cyclic formulations
531 are not implemented.

532 5.2. Vortex convection

533 This numerical test consists of convecting a Lamb-Oseen vortex. The initial vortex is given by the
534 stream function:

$$\Psi(x, y) = \Gamma \exp\left(-\frac{x^2 + y^2}{2R^2}\right), \quad (38)$$

535 where Γ is the vortex strength and R controls the size of the vortex. The resulting velocity distribution
536 is obtained through the velocity stream function relationship:

$$u = U_\infty - \frac{\partial \Psi}{\partial y}, \quad v = V_\infty + \frac{\partial \Psi}{\partial x}. \quad (39)$$

537 Γ is chosen small (0.004) so that the speed of the vortex is much lower than the mean flow speed to test
538 the resolution of the schemes. R is set equal to 0.15. The associated pressure variation follows the radial
539 momentum equation:

$$p - p_\infty = -\frac{\rho \Gamma^2}{2R^2} \exp\left(-\frac{x^2 + y^2}{R^2}\right). \quad (40)$$

540 The convection will be done on the domain $-1 \leq x, y \leq 1$ at the speed $\mathbf{v}_\infty = (U_\infty, V_\infty) = (1, 1)$. The
541 four boundaries are defined as periodic. In this case also, the convection following diagonal direction
542 makes the case really sensitive to multiblock boundary closures and breaks the preferred direction which
543 could exist in the used grids. In order to do not repeat same conclusions as for the linear cases, the
544 number of meshes used for this non linear case is reduced. The notations of methods on figures are
545 unchanged.

546 Something noteworthy is the fact that the initial solution in this case is not simply the point-wise
547 values at the cells centers but really the cell-averaged values of the analytical initial solution. This was
548 not necessary when dealing with linear convection since, because of the linearity, the point-wise values
549 could be seen as cell-averaged values of, of course, a different initial solution. Since in the non-linear case,
550 the solved equations are, without any approximation, equations on cell-averaged values, using point-wise
551 values as cell-averaged values is a supplementary source of errors. This is an important point to get the
552 right order of accuracy of the methods.

553 5.2.1. Effective order of accuracy

554 Numerical orders of the scheme have been retrieved on uniform cartesian and uniform wavy meshes:
555 UNIF, WAVY I and WAVY II. The numerical errors presented are computed using the u and v fields.
556 Actually, it is the sum of the L_2 -error over the two fields. The errors are presented in Tab. 8, Tab. 9,
557 Tab. 10 and Fig. 27. For sake of clarity, for WAVY I and WAVY II meshes only the CART46, CUR46
558 and COMP46 errors have been reported on graphs.

559 On uniform cartesian grids, the schemes are, on average, at least fifth-order accurate. On wavy grids,
560 in general, the errors made with CURxxx methods are inferior to those made with other schemes. One

Mesh size	CART46		CART456	
	Error	Order	Error	Order
16×16	2.57×10^{-5}	-	1.85×10^{-5}	-
32×32	5.79×10^{-7}	5.47	3.51×10^{-7}	5.71
64×64	1.04×10^{-8}	5.79	6.22×10^{-9}	5.81
128×128	2.57×10^{-10}	5.33	2.18×10^{-10}	4.83

Table 8: Numerical mean errors and orders of schemes on UNIF meshes for the vortex convection.

Mesh size	CART46		CUR46		COMP46	
	Error	Order	Error	Order	Error	Order
16×16	6.11×10^{-5}	-	4.23×10^{-5}	-	6.11×10^{-5}	-
32×32	1.17×10^{-6}	5.70	7.12×10^{-7}	5.89	9.97×10^{-7}	5.93
64×64	2.90×10^{-8}	5.33	1.26×10^{-8}	5.82	2.21×10^{-8}	5.49
128×128	9.51×10^{-10}	4.93	2.93×10^{-10}	5.42	9.13×10^{-10}	4.59

Mesh size	CART456		CUR456	
	Error	Order	Error	Order
16×16	6.37×10^{-5}	-	4.27×10^{-5}	-
32×32	4.62×10^{-7}	7.10	4.61×10^{-7}	6.53
64×64	1.50×10^{-8}	4.94	7.56×10^{-9}	5.93
128×128	8.45×10^{-10}	4.14	2.39×10^{-10}	4.98

Table 9: Numerical mean errors and orders of schemes on WAVY I meshes for the vortex convection.

561 can notice that for CURxxx methods, the error is at least close to 5 while for other schemes, it could
562 decrease near to 4. However, the error is higher than the second-order expected and taking into account
563 remarks made in section 3 could improve these results.

564 5.2.2. Stability, dissipation and dispersion properties

565 The vortex position is captured after 25 periods for two types of meshes: WAVY III and RAND.

566 The results obtained on the RAND grid (Fig. 28) and on the WAVY III grid (Fig. 29) confirm
567 conclusions of the linear convection study. The CURxxx schemes have a better behaviour than the
568 CARTxxx and COMP46 schemes.

569 5.2.3. Multiblock computations

570 Some multiblock simulations have been performed using four blocks with the CARTxxx and CURxxx
571 schemes. Fig. 30 shows both the initial and after 50 periods isocontours of vorticity on a UNIF mesh and
572 a WAVY II mesh. It shows that the proposed multiblock treatment does not alter the global precision
573 even if the vortex is convected through the block matching line. The two results obtained on wavy
574 meshes prove that our multiblock strategy works well not only for the FV compact scheme but also for
575 the filtering operator. The $y = 0$ profiles of the v-component of velocity obtained with a monoblock or
576 multiblock calculation match very well (Fig. 31).

577 5.2.4. Conclusion on the vortex convection case

578 These results confirm the one obtained in the linear convection test cases. The proposed schemes are
579 at least of the fourth-order, thus far superior than the formally second-order expected. Even if, it is also

Mesh size	CART46F80.49		CUR46F80.49-NORM-W2		COMP46	
	Error	Order	Error	Order	Error	Order
16×16	6.04×10^{-5}	-	3.22×10^{-5}	-	3.67×10^{-5}	-
32×32	2.39×10^{-5}	1.33	1.15×10^{-5}	1.48	2.71×10^{-5}	0.43
64×64	1.33×10^{-6}	4.17	3.41×10^{-7}	5.07	1.51×10^{-6}	4.16
128×128	1.58×10^{-8}	6.39	3.13×10^{-9}	6.76	1.59×10^{-8}	6.56
256×256	5.76×10^{-10}	4.77	9.91×10^{-11}	4.98	7.79×10^{-10}	4.35

Mesh size	CART456F80.49		CUR46F80.49-NORM-W2	
	Error	Order	Error	Order
16×16	6.04×10^{-5}	-	3.47×10^{-5}	-
32×32	2.36×10^{-5}	1.35	1.17×10^{-5}	1.56
64×64	1.27×10^{-6}	4.21	4.05×10^{-7}	4.85
128×128	1.31×10^{-8}	6.59	3.76×10^{-9}	6.75
256×256	5.61×10^{-10}	4.54	1.01×10^{-10}	5.21

Table 10: Numerical mean errors and orders of schemes on WAVY II meshes for the vortex convection.

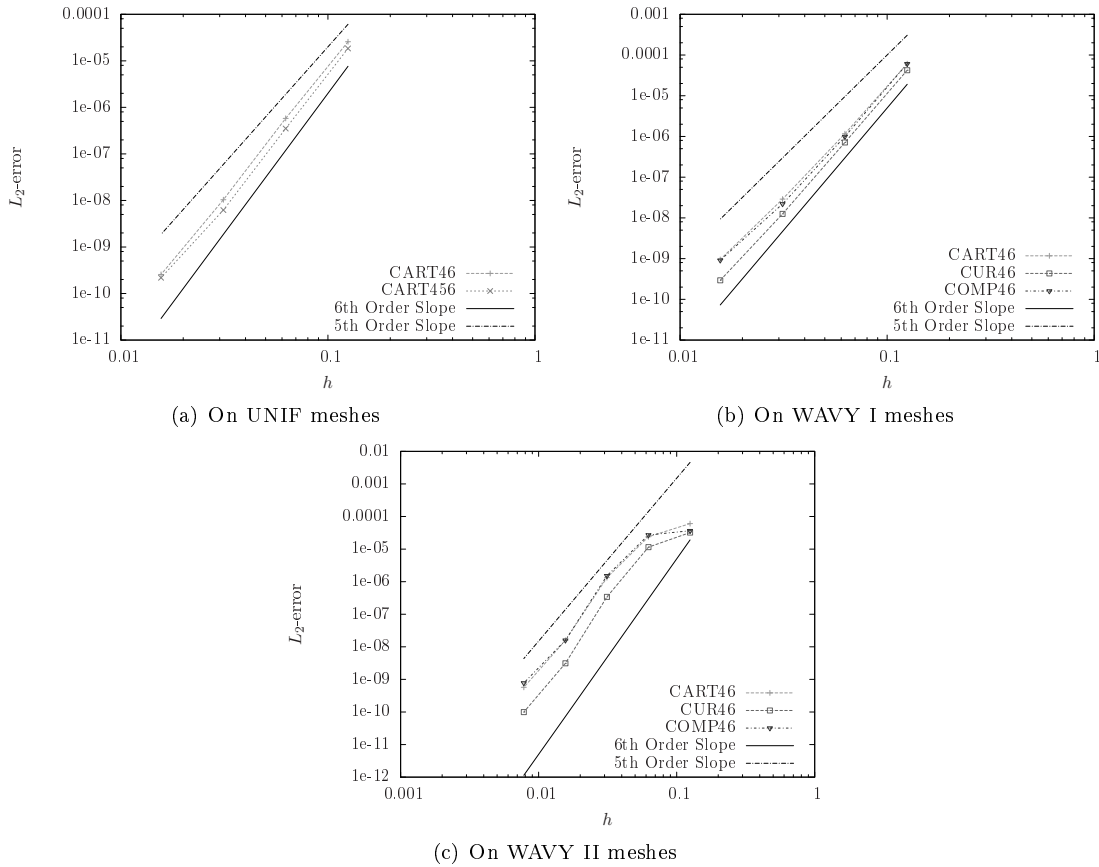


Figure 27: Evolution of the errors following the mesh size for the 2D vortex convection.

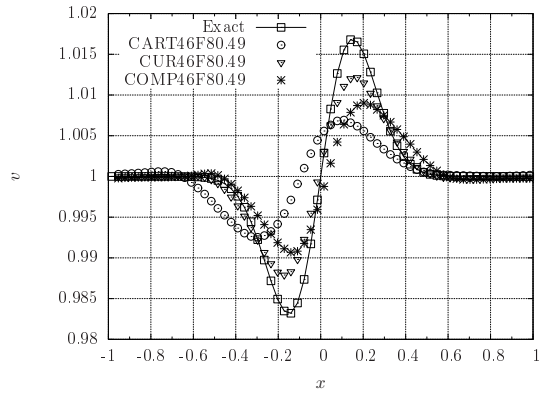


Figure 28: $y = 0$ profile of the v -component of a vortex velocity on a RAND mesh after 25 periods.

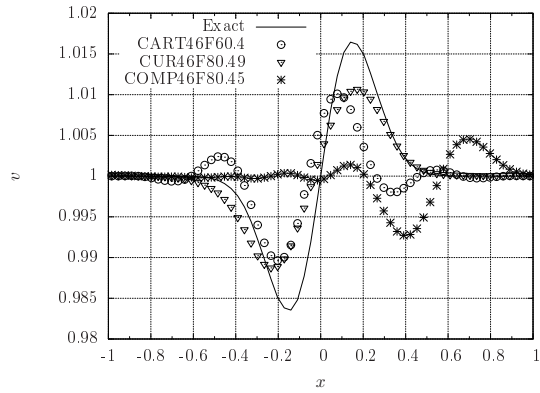
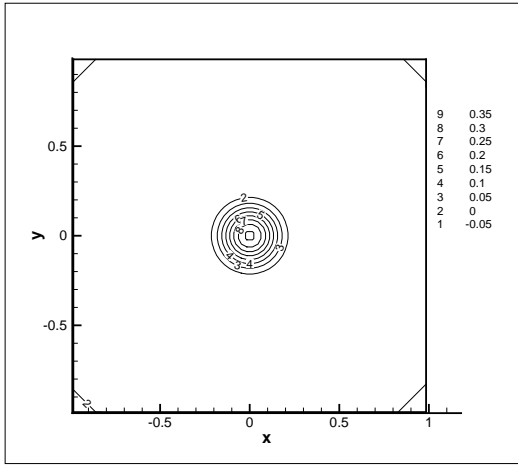
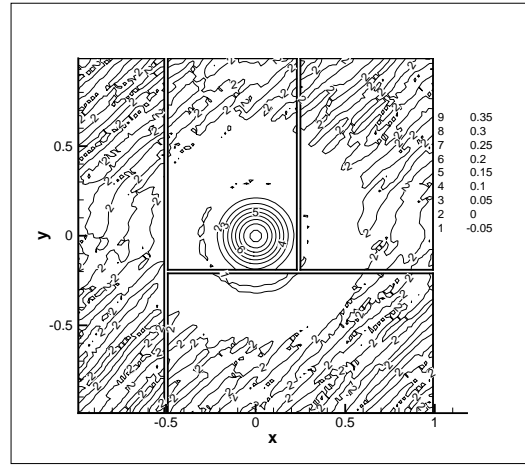


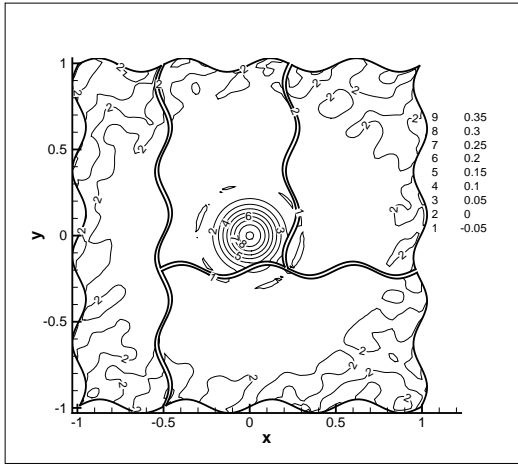
Figure 29: $y = 0$ profile of the v -component of a vortex velocity on a WAVY III mesh after 25 periods: the CUR46 method uses the GEN frame.



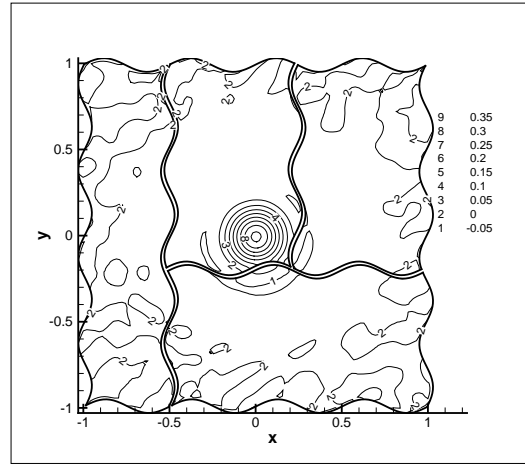
(a) Exact solution



(b) On a splitted UNIF grid using CART456 scheme

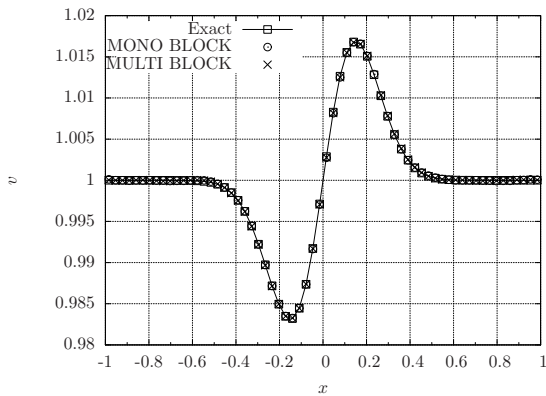


(c) On a splitted WAVY I grid using CART46+F60.49 scheme

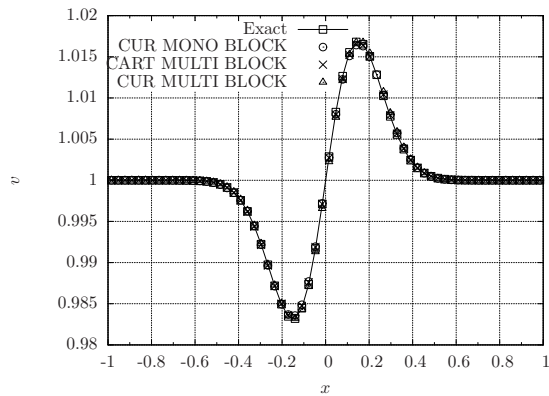


(d) On a splitted WAVY I grid using CUR46+F60.49 scheme

Figure 30: Vorticity isocontours after 50 periods of vortex convection in multi-blocks configuration.



(a) Uniform mesh using the CART456 scheme



(b) Wavy mesh using CUR456+F60.49 scheme

Figure 31: $y = 0$ profile of the v -component of the velocity after 50 periods of vortex convection in mono- and multi-block configuration.

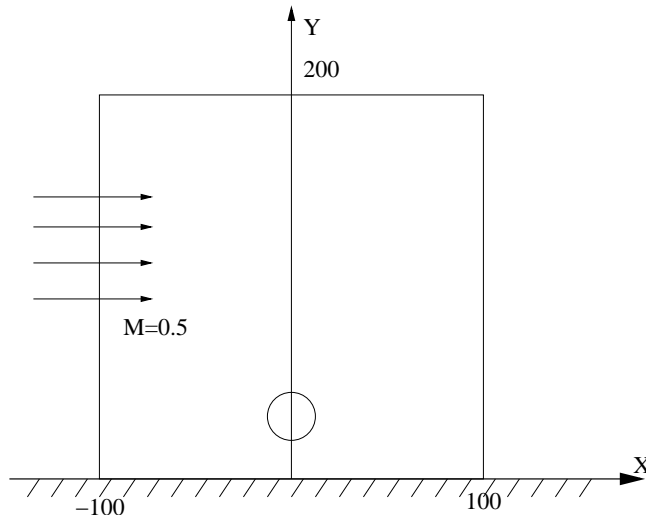


Figure 32: *Pressure wave reflection on wall boundary test case.*

580 the case for the COMP46 method, CURxxx methods are obviously more accurate. It is also interesting
 581 to note that the multiblock computations do not deteriorate the solution for long time simulations.

582 5.3. *Acoustic scattering by a plane wall*

583 This test case is the first problem of the fourth category of the first workshop ICASE-NASA [9]. It
 584 consists of the reflection of a 2D Gaussian pressure pulse on a wall boundary. This test case aims also
 585 to test the wall boundary scheme. The configuration is presented on Fig. 32. The reference values are
 586 the same as those used by Gloerfelt [6]: $P_\infty = 1 \times 10^5$ Pa, $\rho_\infty = 1.22\text{kg}\cdot\text{m}^{-3}$. The acoustic perturbations
 587 introduced is given by:

$$p' = \exp \left[-\frac{\ln 2}{25} (x^2 + (y - 25)^2) \right]. \quad (41)$$

588 Computations are carried out on a randomly perturbed mesh (RAND) with 100×100 cells.
 589 The inflow characteristic boundary condition of Poinot and Lele [20] is used. The outflow boundaries
 590 are computed using Tam and Dong [24] acoustic radiative condition. Numerical results are compared
 591 with the exact solution.

592 A profile of the acoustic pressure along the axis $x = y$ is shown on Fig. 33. CUR46 and COMP46 schemes
 593 behave better than CART46 and CEN4 schemes. CUR46 scheme is slightly better than COMP46 in
 594 term of dissipation. CEN4 is obviously the worst schemes. The test case was pretty difficult since it has
 595 been realized using a non linear code while it is generally realized using linearized Euler equations. The
 596 success of the test confirms that the schemes are able to propagate properly an acoustic wave of 10^{-5}
 597 magnitude lower than the aerodynamic pressure.

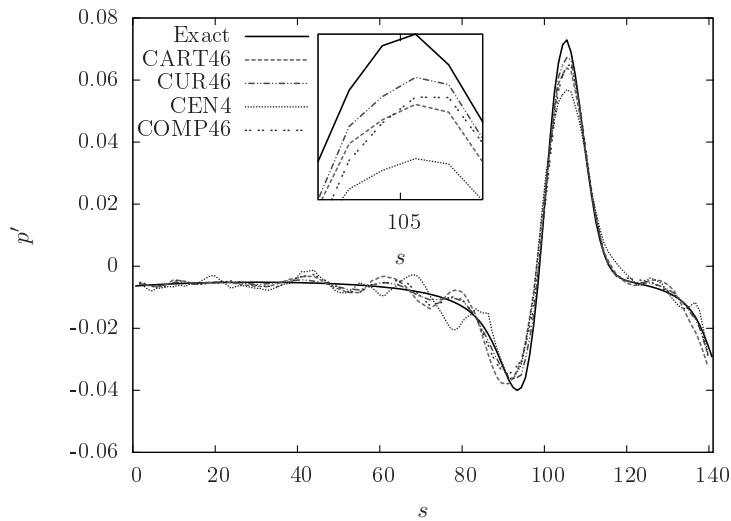


Figure 33: Profile of the acoustic pressure along the axis $x = y$ at $t = 100$: all methods are combined with the *F80.49* filter.

598 6. Conclusion

599 High order compact interpolation methods have been presented in order to develop high order finite-
600 volumes methods using small stencils on arbitrary curvilinear schemes. The first approach (CARTxxx
601 methods) is a 1D-like scheme considering a mesh line as a 1D direction and using the curvilinear abscissa
602 on this mesh line. The second approach (CURxxx), more general, uses supplementary cells to account
603 for transverse derivatives terms and kinetic moments to account for the cells shape and size. This latter
604 approach is developed in a local frame and is sixth-order in a preferred direction of this local frame.
605 It is worth noting that both approaches match on cartesian grids. Considering parallel calculations
606 requirements, three boundary closures for multiblock or periodic boundaries have been studied and two
607 have been chosen for implementation in the solver **elsA**. The boundary closure which uses an upwind
608 formulation of the flux at the second interface shows a good behaviour in terms of stability and dispersion
609 on cartesian grids. This is no longer the case on curvilinear grids. This fact shows some limits of
610 generalizing a 1D theoretical analysis to multidimensional problems.

611 Numerical tests of convection have been realized both in linear and non-linear cases to observe
612 stability and dispersion properties of the different schemes. These tests have highlighted the need to
613 stabilize the methods for long computations. This have been done using high-order compact filters in
614 computational space. For most of the test cases done, filters behave very well although they are done in
615 the computational space. Moreover, even with the filtering, the effective order of accuracy of schemes
616 is, at least four for the CARTxxx methods and five for the CURxxx ones for two and three dimensional
617 flows.

618 Although the scheme using compact interpolation with constant coefficients (COMP46) behaves very well
619 on uniform cartesian and curvilinear grids, when dealing with non-uniformities (irregularity of cells size),
620 CARTxxx and CURxxx give much better results in terms of dispersion and dissipation. Moreover, when
621 cells shape and mesh line directions strongly vary, CURxxx schemes are clearly superior to CARTxxx

622 ones. These latter schemes could, in some of those cases, behaves worse than COMP46 schemes.
 623 For CURxxx methods, it is shown that the choice of the local frame could help to get more stability, low
 624 dissipation and dispersion effects.

625 An acoustic scattering benchmark problem has also been solved with the proposed methods. This test
 626 has shown that the different methods can handle problems requiring high precision and good spectral
 627 resolution, and thus constitute an interesting building block for aeroacoustics applications in the future.

628 In the present paper, the extension to non-linear equations has been rapidly discussed but need a
 629 more deeper investigation. This work is on going. For the test cases presented, the different approaches
 630 which could be considered do not make a valuable difference. It would be interesting to analyze them
 631 using, for example, an isotropic homogenous turbulence simulation with a Large Eddy Simulation (LES)
 632 approach. Along these lines, it could be interesting to investigate if forcing the usage of supplementary
 633 cells even on cartesian grids could improve the isotropy properties of scheme and thus their ability to
 634 perform LES.

635 A. Sixth-order compact interpolation for a cartesian mesh

636 This section presents the derivation of the coefficients used for the cartesian-like scheme (Eq. (8))
 637 which is sixth-order on a cartesian mesh. Therefore, it is assumed that the mesh is cartesian, which
 638 means that the i mesh lines follow a x' direction and the j mesh lines a y' direction such that (x', y')
 639 is an orthonormal frame. For sake of convenience, it is assumed that these directions x' and y' match
 640 with the usual coordinate directions x and y . Thus, when introducing the Taylor developments, it is not
 641 necessary to integrate over the y direction (neither over the z direction in the 3D case). Indeed, Eq. (8)
 642 leads to:

$$\begin{aligned}
 \int_{-\frac{\Delta y}{2}}^{\frac{\Delta y}{2}} (\alpha u(x_{i-1/2,j}, y) + u(x_{i+1/2,j}, y) + \beta u(x_{i+3/2,j}, y)) dy \approx \int_{-\frac{\Delta y}{2}}^{\frac{\Delta y}{2}} \left(a \frac{1}{h_{i-1}} \int_{x_{i-3/2,j}}^{x_{i-1/2,j}} u(x, y) dx \right. \\
 \left. + b \frac{1}{h_i} \int_{x_{i-1/2,j}}^{x_{i+1/2,j}} u(x, y) dx + c \frac{1}{h_{i+1}} \int_{x_{i+1/2,j}}^{x_{i+3/2,j}} u(x, y) dx + d \frac{1}{h_{i+2}} \int_{x_{i+3/2,j}}^{x_{i+5/2,j}} u(x, y) dx \right) dy,
 \end{aligned} \tag{42}$$

643 where Δy is the size of the iso-meshline j following the y direction. Hence, it is sufficient to find the
 644 coefficients $\alpha, \beta, a, b, c, d$ such that:

$$\begin{aligned}
 \alpha u(x_{i-1/2,j}, y) + u(x_{i+1/2,j}, y) + \beta u(x_{i+3/2,j}, y) \approx a \frac{1}{h_{i-1}} \int_{x_{i-3/2,j}}^{x_{i-1/2,j}} u(x, y) dx + b \frac{1}{h_i} \int_{x_{i-1/2,j}}^{x_{i+1/2,j}} u(x, y) dx \\
 + c \frac{1}{h_{i+1}} \int_{x_{i+1/2,j}}^{x_{i+3/2,j}} u(x, y) dx + d \frac{1}{h_{i+2}} \int_{x_{i+3/2,j}}^{x_{i+5/2,j}} u(x, y) dx.
 \end{aligned} \tag{43}$$

645 This shows that it is sufficient to derive a sixth-order approximation just in the x -direction. To do so, it
 646 is necessary to match the coefficient of the derivatives until the fifth-order derivative in the x -direction
 647 of the left and right hand sides of the approximation Eq. (43).

There are detailed the coefficients of the derivatives for the left hand side of Eq. (43):

$$\begin{aligned}
0^{\text{th}} \text{ order} & : 1 + \alpha + \beta, \\
1^{\text{st}} \text{ order } \frac{\partial}{\partial x} & : -\alpha h_i + \beta h_{i+1}, \\
2^{\text{nd}} \text{ order } \frac{\partial^2}{\partial x^2} & : \frac{1}{2}\alpha h_i^2 + \frac{1}{2}\beta h_{i+1}^2, \\
3^{\text{rd}} \text{ order } \frac{\partial^3}{\partial x^3} & : -\frac{1}{6}\alpha h_i^3 + \frac{1}{6}\beta h_{i+1}^3, \\
4^{\text{th}} \text{ order } \frac{\partial^4}{\partial x^4} & : \frac{1}{24}\alpha h_i^4 + \frac{1}{24}\beta h_{i+1}^4, \\
5^{\text{th}} \text{ order } \frac{\partial^5}{\partial x^5} & : -\frac{1}{120}\alpha h_i^5 + \frac{1}{120}\beta h_{i+1}^5,
\end{aligned} \tag{44}$$

where $h_{i'} = x_{i'+1/2} - x_{i'-1/2}$ is the distance between the interfaces $i' - 1/2$ and $i' + 1/2$.

The coefficients of the derivatives for the right hand side are:

$$\begin{aligned}
0 \text{ order} & : a + b + c + d, \\
1^{\text{st}} \text{ order } \frac{\partial}{\partial x} & : \frac{1}{2} [-a(2h_i + h_{i-1}) - bh_i + ch_{i+1} + d(2h_{i+1} + h_{i+2})], \\
2^{\text{nd}} \text{ order } \frac{\partial^2}{\partial x^2} & : \frac{1}{6} \left[a \frac{1}{h_{i-1}} ((h_i + h_{i-1})^3 - h_i^3) + bh_i^2 + ch_{i+1}^2 + d \frac{1}{h_{i+2}} ((h_{i+1} + h_{i+2})^3 - h_{i+1}^3) \right], \\
3^{\text{rd}} \text{ order } \frac{\partial^3}{\partial x^3} & : \frac{1}{24} \left[a \frac{1}{h_{i-1}} (h_i^4 - (h_i + h_{i-1})^4) - bh_i^3 + ch_{i+1}^3 + d \frac{1}{h_{i+2}} ((h_{i+1} + h_{i+2})^4 - h_{i+1}^4) \right], \\
4^{\text{th}} \text{ order } \frac{\partial^4}{\partial x^4} & : \frac{1}{120} \left[a \frac{1}{h_{i-1}} ((h_i + h_{i-1})^5 - h_i^5) + bh_i^4 + ch_{i+1}^4 + d \frac{1}{h_{i+2}} ((h_{i+1} + h_{i+2})^5 - h_{i+1}^5) \right], \\
5^{\text{th}} \text{ order } \frac{\partial^5}{\partial x^5} & : \frac{1}{720} \left[a \frac{1}{h_{i-1}} (h_i^6 - (h_i + h_{i-1})^6) - bh_i^5 + ch_{i+1}^5 + d \frac{1}{h_{i+2}} ((h_{i+1} + h_{i+2})^6 - h_{i+1}^6) \right].
\end{aligned} \tag{45}$$

Solving the system results in finding the following coefficients:

$$\alpha = \frac{h_{i+1}^2 (h_{i-1} + h_i)(h_{i+1} + h_{i+2})}{h_{i-1}(h_i + h_{i+1})^2(h_i + h_{i+1} + h_{i+2})}, \tag{46}$$

$$\beta = \frac{h_i^2 (h_{i-1} + h_i)(h_{i+1} + h_{i+2})}{(h_i + h_{i+1})^2(h_{i-1} + h_i + h_{i+1})h_{i+2}}, \tag{47}$$

$$a = \frac{h_i^2 h_{i+1}^2 (h_{i+1} + h_{i+2})}{h_{i-1}(h_{i-1} + h_i)(h_{i-1} + h_i + h_{i+1})^2(h_{i-1} + h_i + h_{i+1} + h_{i+2})}, \tag{48}$$

$$\begin{aligned}
b = & \frac{h_{i+1}^2}{h_{i-1}^2} \left(\frac{2h_{i-1}h_i(h_{i-1} + h_i)}{(h_i + h_{i+1})^3} + \frac{(2h_{i-1} - h_i)(h_{i-1} + h_i)}{(h_i + h_{i+1})^2} \right. \\
& + \frac{(h_{i-1} + h_i)(h_{i-1} + h_i + h_{i+1})^2}{h_i^3} - \frac{h_{i-1}h_i^2(h_{i-1} + h_i)}{(h_i + h_{i+1})^2(h_{i-1} + h_i + h_{i+1})^2} \\
& + \frac{h_i(h_{i-1} + h_i)(h_i(h_i + h_{i+1}) - h_{i-1}(3h_i + h_{i+1}))}{(h_i + h_{i+1})^3(h_i + h_{i+1} + h_{i+2})} \\
& \left. - \frac{h_i^3}{(h_{i-1} + h_i + h_{i+1})^2(h_{i-1} + h_i + h_{i+1} + h_{i+2})} \right), \tag{49}
\end{aligned}$$

$$\begin{aligned}
c = & \frac{h_i^2}{h_{i+2}^2} \left(\frac{2h_{i+2}h_{i+1}(h_{i+1} + h_{i+2})}{(h_i + h_{i+1})^3} + \frac{(-h_{i+1} + 2h_{i+2})(h_{i+1} + h_{i+2})}{(h_i + h_{i+1})^2} \right. \\
& + \frac{h_{i+1}^3}{h_{i+2}^2} \frac{(h_{i+1} + h_{i+2})(h_i + h_{i+1} + h_{i+2})^2}{h_{i+1}(h_{i+1} + h_{i+2})(h_{i+1}(h_i + h_{i+1}) - (h_i + 3h_{i+1})h_{i+2})} \\
& \left. - \frac{(h_i + h_{i+1})^2(h_i + h_{i+1} + h_{i+2})^2}{(h_i + h_{i+1})^3(h_{i-1} + h_i + h_{i+1})} \right) \\
& - \frac{(h_i + h_{i+1} + h_{i+2})^2(h_{i-1} + h_i + h_{i+1} + h_{i+2})}{h_{i+1}^3}, \tag{50}
\end{aligned}$$

$$d = \frac{h_i^2 h_{i+1}^2 (h_{i-1} + h_i)}{h_{i+2}(h_{i+1} + h_{i+2})(h_i + h_{i+1} + h_{i+2})^2(h_{i-1} + h_i + h_{i+1} + h_{i+2})}. \tag{51}$$

657 B. Sixth-order compact interpolation for a curvilinear mesh

658 In this section, considering Eq. (5), details are presented about how the coefficients of the curvilinear
659 scheme using transverse derivatives and local frame are determined. For sake of simplicity all develop-
660 ments are done for the 2D case. For sake of convenience the local reference frame (x', y') is assumed to
661 match with the usual frame (x, y) . All equations written there are retrieved in (x', y') just by replacing
662 x and y by x' and y' respectively. The interpolation is done around the interface $(i + 1/2, j)$. There are
663 some definitions on an interface $(i' + 1/2, j')$:

$$\begin{aligned}
x_{i'+1/2, j'} &= \frac{1}{S_{i'+1/2, j'}} \int_{S_{i'+1/2, j'}} x dS, \\
y_{i'+1/2, j'} &= \frac{1}{S_{i'+1/2, j'}} \int_{S_{i'+1/2, j'}} y dS, \\
J_{i'+1/2, j'}^{x^n y^m} &= \frac{1}{S_{i'+1/2, j'}} \int_{S_{i'+1/2, j'}} (x - x_{i'+1/2})^n (y - y_{i'+1/2})^m dS, \\
\delta_{i'+1/2, j'}^x &= x_{i'+1/2, j'} - x_{i+1/2, j}, \\
\delta_{i'+1/2, j'}^y &= y_{i'+1/2, j'} - y_{i+1/2, j}.
\end{aligned}$$

664 Since, just interfaces on the j -th i mesh line are considered, interfaces underscripts are just $i' + 1/2$
665 instead of $(i' + 1/2, j)$. With same considerations, coefficients $\alpha_{i+1/2, j, k}$, $\beta_{i+1/2, j, k}$, and $a_{i+1/2, j, k}^{i+1/2, j, k}$ are just
666 noted α , β , and $a_{i+1/2, j}$. There are now equivalent definitions for a cell (i, j) :

$$\begin{aligned}
x_{i', j'} &= \frac{1}{V_{i', j'}} \int_{V_{i', j'}} x dV, \\
y_{i', j'} &= \frac{1}{V_{i', j'}} \int_{V_{i', j'}} y dV, \\
J_{i', j'}^{x^n y^m} &= \frac{1}{V_{i', j'}} \int_{V_{i', j'}} (x - x_{i', j'})^n (y - y_{i', j'})^m dV, \\
\delta_{i', j'}^x &= x_{i', j'} - x_{i+1/2}, \\
\delta_{i', j'}^y &= y_{i', j'} - y_{i+1/2}.
\end{aligned}$$

667 One can note that $J_{i', j'}^x = J_{i', j'}^y = 0$.

668 The Taylor series of a function $u(x, y)$ at the point (x_0, y_0) is

$$u(x, y) = \sum_{m=0}^{\infty} \sum_{n=0}^{\infty} \frac{\partial^{m+n}}{\partial x^m \partial y^n} u(x_0, y_0) \frac{1}{m!} \frac{1}{n!} (x - x_0)^m (y - y_0)^n. \tag{52}$$

669 So, the mean value of u on a domain Ω is

$$\bar{u}_\Omega = \frac{1}{|\Omega|} \int_\Omega u d\Omega = \frac{1}{|\Omega|} \int_\Omega \left[\sum_{m=0}^{\infty} \sum_{n=0}^{\infty} \frac{\partial^m}{\partial x^m} \frac{\partial^n}{\partial y^n} u(x_0, y_0) \frac{1}{m!} \frac{1}{n!} (x - x_0)^m (y - y_0)^n \right] d\Omega. \quad (53)$$

670 When introducing Taylor series around $x_{i+1/2}$, on the left hand side, coefficients of the derivatives which
 671 will be cancelled are:

$$\begin{aligned} 0^{\text{th}} \text{ order} & : 1 + \alpha + \beta, \\ 1^{\text{st}} \text{ order } \frac{\partial}{\partial x} & : \alpha \delta_{i-1/2}^x + \beta \delta_{i+3/2}^x, \\ & \frac{\partial}{\partial y} : \alpha \delta_{i-1/2}^y + \beta \delta_{i+3/2}^y, \\ 2^{\text{nd}} \text{ order } \frac{\partial^2}{\partial x^2} & : \frac{1}{2} \alpha \left((\delta_{i-1/2}^x)^2 + J_{i-1/2}^{x^2} \right) + \frac{1}{2} J_{i+1/2}^{x^2} + \frac{1}{2} \beta \left((\delta_{i+3/2}^x)^2 + J_{i+3/2}^{x^2} \right), \\ & \frac{\partial^2}{\partial y^2} : \frac{1}{2} \alpha \left((\delta_{i-1/2}^y)^2 + J_{i-1/2}^{y^2} \right) + \frac{1}{2} J_{i+1/2}^{y^2} + \frac{1}{2} \beta \left((\delta_{i+3/2}^y)^2 + J_{i+3/2}^{y^2} \right), \\ & \frac{\partial^2}{\partial x \partial y} : \alpha \left(\delta_{i-1/2}^x \delta_{i-1/2}^y + J_{i-1/2}^{xy} \right) + J_{i+1/2}^{xy} + \beta \left(\delta_{i+3/2}^x \delta_{i+3/2}^y + J_{i+3/2}^{xy} \right), \\ 3^{\text{rd}} \text{ order } \frac{\partial^3}{\partial x^3} & : \frac{1}{6} \alpha \left((\delta_{i-1/2}^x)^3 + 3 \delta_{i-1/2}^x J_{i-1/2}^{x^2} + J_{i-1/2}^{x^3} \right) + \frac{1}{6} J_{i+1/2}^{x^3} + \frac{1}{6} \beta \left((\delta_{i+3/2}^x)^3 + 3 \delta_{i+3/2}^x J_{i+3/2}^{x^2} + J_{i+3/2}^{x^3} \right), \\ & \frac{\partial^3}{\partial y^3} : \frac{1}{6} \alpha \left((\delta_{i-1/2}^y)^3 + 3 \delta_{i-1/2}^y J_{i-1/2}^{y^2} + J_{i-1/2}^{y^3} \right) + \frac{1}{6} J_{i+1/2}^{y^3} + \frac{1}{6} \beta \left((\delta_{i+3/2}^y)^3 + 3 \delta_{i+3/2}^y J_{i+3/2}^{y^2} + J_{i+3/2}^{y^3} \right), \\ & \frac{\partial^3}{\partial x^2 \partial y} : \frac{1}{2} \alpha \left((\delta_{i-1/2}^x)^2 \delta_{i-1/2}^y + 2 \delta_{i-1/2}^x J_{i-1/2}^{xy} + \delta_{i-1/2}^y J_{i-1/2}^{x^2} + J_{i-1/2}^{x^2 y} \right) + \frac{1}{2} J_{i+1/2}^{x^2 y} \\ & \quad + \frac{1}{2} \beta \left((\delta_{i+3/2}^x)^2 \delta_{i+3/2}^y + 2 \delta_{i+3/2}^x J_{i+3/2}^{xy} + \delta_{i+3/2}^y J_{i+3/2}^{x^2} + J_{i+3/2}^{x^2 y} \right), \\ & \frac{\partial^3}{\partial x \partial y^2} : \frac{1}{2} \alpha \left(\delta_{i-1/2}^x (\delta_{i-1/2}^y)^2 + 2 \delta_{i-1/2}^y J_{i-1/2}^{xy} + \delta_{i-1/2}^x J_{i-1/2}^{y^2} + J_{i-1/2}^{xy^2} \right) + \frac{1}{2} J_{i+1/2}^{xy^2} \\ & \quad + \frac{1}{2} \beta \left(\delta_{i+3/2}^x (\delta_{i+3/2}^y)^2 + 2 \delta_{i+3/2}^y J_{i+3/2}^{xy} + \delta_{i+3/2}^x J_{i+3/2}^{y^2} + J_{i+3/2}^{xy^2} \right), \\ 4^{\text{th}} \text{ order} & \text{ transverse terms will not be used} \\ & \frac{\partial^4}{\partial x^4} : \frac{1}{24} \alpha \left((\delta_{i-1/2}^x)^4 + 6 (\delta_{i-1/2}^x)^2 J_{i-1/2}^{x^2} + 4 \delta_{i-1/2}^x J_{i-1/2}^{x^3} + J_{i-1/2}^{x^4} \right) + \frac{1}{24} J_{i+1/2}^{x^4} \\ & \quad + \frac{1}{24} \beta \left((\delta_{i+3/2}^x)^4 + 6 (\delta_{i+3/2}^x)^2 J_{i+3/2}^{x^2} + 4 \delta_{i+3/2}^x J_{i+3/2}^{x^3} + J_{i+3/2}^{x^4} \right), \\ 5^{\text{th}} \text{ order} & \text{ transverse terms will not be used} \\ & \frac{\partial^5}{\partial x^5} : \frac{1}{120} \alpha \left((\delta_{i-1/2}^x)^5 + 10 (\delta_{i-1/2}^x)^3 J_{i-1/2}^{x^2} + 10 (\delta_{i-1/2}^x)^2 J_{i-1/2}^{x^3} + 5 \delta_{i-1/2}^x J_{i-1/2}^{x^4} + J_{i-1/2}^{x^5} \right) + \frac{1}{120} J_{i+1/2}^{x^5} \\ & \quad + \frac{1}{120} \beta \left((\delta_{i+3/2}^x)^5 + 10 (\delta_{i+3/2}^x)^3 J_{i+3/2}^{x^2} + 10 (\delta_{i+3/2}^x)^2 J_{i+3/2}^{x^3} + 5 \delta_{i+3/2}^x J_{i+3/2}^{x^4} + J_{i+3/2}^{x^5} \right). \end{aligned} \quad (54)$$

672 On the right hand side, the following coefficients are found:

$$\begin{aligned}
0 \text{ order} & : \sum_{l=-m}^{l=n} \sum_{p=-q}^{p=r} a_{l,p}, \\
1^{\text{st}} \text{ order } \frac{\partial}{\partial x} & : \sum_{l=-m}^{l=n} \sum_{p=-q}^{p=r} a_{l,p} \delta_{i+l,j+p}^x, \\
\frac{\partial}{\partial y} & : \sum_{l=-m}^{l=n} \sum_{p=-q}^{p=r} a_{l,p} \delta_{i+l,j+p}^y, \\
2^{\text{nd}} \text{ order } \frac{\partial^2}{\partial x^2} & : \frac{1}{2} \sum_{l=-m}^{l=n} \sum_{p=-q}^{p=r} a_{l,p} \left((\delta_{i+l,j+p}^x)^2 + J_{i+l,j+p}^{x^2} \right), \\
\frac{\partial^2}{\partial y^2} & : \frac{1}{2} \sum_{l=-m}^{l=n} \sum_{p=-q}^{p=r} a_{l,p} \left((\delta_{i+l,j+p}^y)^2 + J_{i+l,j+p}^{y^2} \right), \\
\frac{\partial^2}{\partial x \partial y} & : \sum_{l=-m}^{l=n} \sum_{p=-q}^{p=r} a_{l,p} \left(\delta_{i+l,j+p}^x \delta_{i+l,j+p}^y + J_{i+l,j+p}^{xy} \right), \\
3^{\text{rd}} \text{ order } \frac{\partial^3}{\partial x^3} & : \frac{1}{6} \sum_{l=-m}^{l=n} \sum_{p=-q}^{p=r} a_{l,p} \left((\delta_{i+l,j+p}^x)^3 + 3\delta_{i+l,j+p}^x J_{i+l,j+p}^{x^2} + J_{i+l,j+p}^{x^3} \right), \\
\frac{\partial^3}{\partial y^3} & : \frac{1}{6} \sum_{l=-m}^{l=n} \sum_{p=-q}^{p=r} a_{l,p} \left((\delta_{i+l,j+p}^y)^3 + 3\delta_{i+l,j+p}^y J_{i+l,j+p}^{y^2} + J_{i+l,j+p}^{y^3} \right), \\
\frac{\partial^3}{\partial x^2 \partial y} & : \frac{1}{2} \sum_{l=-m}^{l=n} \sum_{p=-q}^{p=r} a_{l,p} \left((\delta_{i+l,j+p}^x)^2 \delta_{i+l,j+p}^y + 2\delta_{i+l,j+p}^x J_{i+l,j+p}^{xy} + \delta_{i+l,j+p}^y J_{i+l,j+p}^{x^2} + J_{i+l,j+p}^{x^2 y} \right), \\
\frac{\partial^3}{\partial x \partial y^2} & : \frac{1}{2} \sum_{l=-m}^{l=n} \sum_{p=-q}^{p=r} a_{l,p} \left(\delta_{i+l,j+p}^x (\delta_{i+l,j+p}^y)^2 + 2\delta_{i+l,j+p}^y J_{i+l,j+p}^{xy} + \delta_{i+l,j+p}^x J_{i+l,j+p}^{y^2} + J_{i+l,j+p}^{xy^2} \right), \\
4^{\text{th}} \text{ order} & \text{ transverse terms will not be used} \\
\frac{\partial^4}{\partial x^4} & : \frac{1}{24} \sum_{l=-m}^{l=n} \sum_{p=-q}^{p=r} a_{l,p} \left((\delta_{i+l,j+p}^x)^4 + 6(\delta_{i+l,j+p}^x)^2 J_{i+l,j+p}^{x^2} + 4\delta_{i+l,j+p}^x J_{i+l,j+p}^{x^3} + J_{i+l,j+p}^{x^4} \right), \\
5^{\text{th}} \text{ order} & \text{ transverse terms will not be used} \\
\frac{\partial^5}{\partial x^5} & : \frac{1}{120} \sum_{l=-m}^{l=n} \sum_{p=-q}^{p=r} a_{l,p} \left((\delta_{i+l,j+p}^x)^5 + 10(\delta_{i+l,j+p}^x)^3 J_{i+l,j+p}^{x^2} + 10(\delta_{i+l,j+p}^x)^2 J_{i+l,j+p}^{x^3} + 5\delta_{i+l,j+p}^x J_{i+l,j+p}^{x^4} + J_{i+l,j+p}^{x^5} \right),
\end{aligned} \tag{55}$$

It is now necessary to prove that this method matches with the cartesian-like method when a cartesian grid is considered. To do so, for sake of simplicity, let be considered a 2D case with notations introduced in section 2.2.3 and in appendix A. It is clear that the three types of local reference frames introduced are the same in this case. It is still assumed that the preferred direction for the interface $(i+1/2, j)$ is the x direction. The aim is to show that the coefficients $X = \left(\underbrace{\alpha, \beta, a, b, c, d}_{X_1}, \underbrace{e, f, g, h}_{X_2} \right)$ with $\alpha, \beta, a, b, c, d$ defined as in appendix A and $e = f = g = h = 0$ is the one which verify the equations defined for the CUR_{xxx} method.

Considering that coefficients $\alpha, \beta, a, b, c, d$ are determined by matching coefficients of derivatives in the x directions involving in Eq. (42), it is clear that:

$$(A \ B)X = 0.$$

673 This could be checked using the following expressions of kinetic moments:

$$\begin{aligned}
\delta_{i-1/2,j}^x &= -h_i \text{ and } \delta_{i-1/2,j}^y = 0 \\
\delta_{i+3/2,j}^x &= h_{i+1} \text{ and } \delta_{i+3/2,j}^y = 0 \\
J_{i-1/2,j}^{x^m y^n} &= J_{i+1/2,j}^{x^m y^n} = J_{i+3/2,j}^{x^m y^n} = 0, \forall m > 0 \\
J_{i-1/2,j}^{y^2} &= J_{i+1/2,j}^{y^2} = J_{i+3/2,j}^{y^2} = \Delta y^2/12 \\
J_{i-1/2,j}^{y^3} &= J_{i+1/2,j}^{y^3} = J_{i+3/2,j}^{y^3} = 0
\end{aligned}$$

674

$$\begin{aligned}
\delta_{i-1,j}^x &= -(h_{i-1}/2 + h_i), \delta_{i,j}^x = -h_i/2, \delta_{i+1,j}^x = h_{i+1}/2 \text{ and } \delta_{i+2,j}^x = (h_{i+1} + h_{i+2}/2), \\
\delta_{i-1,j}^y &= \delta_{i,j}^y = \delta_{i+1,j}^y = \delta_{i+2,j}^y = 0, \\
J_{i-1,j}^{x^m y^n} &= J_{i,j}^{x^m y^n} = J_{i+1,j}^{x^m y^n} = J_{i+2,j}^{x^m y^n} = 0, \forall m, n \text{ if } m \text{ or } n \text{ is odd,} \\
J_{i-1,j}^{x^2} &= h_{i-1}^2/12, J_{i,j}^{x^2} = h_i^2/12, J_{i+1,j}^{x^2} = h_{i+1}^2/12 \text{ and } J_{i+2,j}^{x^2} = h_{i+2}^2/12 \\
J_{i-1,j}^{x^4} &= h_{i-1}^4/80, J_{i,j}^{x^4} = h_i^4/80, J_{i+1,j}^{x^4} = h_{i+1}^4/80 \text{ and } J_{i+2,j}^{x^4} = h_{i+2}^4/80 \\
J_{i-1,j}^{x^5} &= J_{i,j}^{x^5} = J_{i+1,j}^{x^5} = J_{i+2,j}^{x^5} = 0 \\
J_{i-1,j}^{y^2} &= J_{i,j}^{y^2} = J_{i+1,j}^{y^2} = J_{i+2,j}^{y^2} = \Delta y^2/12 \\
J_{i-1,j}^{y^4} &= J_{i,j}^{y^4} = J_{i+1,j}^{y^4} = J_{i+2,j}^{y^4} = \Delta y^4/80
\end{aligned}$$

675 where Δy is the length following the y direction of the interface $(i + 1/2, j)$. It could also be checked
676 that the given vector X verify all the relations given by the transverse derivatives. Indeed, the following
677 relations are obtained:

$$\begin{aligned}
\frac{\partial}{\partial y} &: 0 = e\delta_{i,j-1}^y + f\delta_{i,j+1}^y + g\delta_{i+1,j-1}^y + h\delta_{i+1,j+1}^y \\
\frac{\partial^2}{\partial y^2} &: \frac{\Delta y^2}{24}(\alpha + 1 + \beta) = \frac{\Delta y^2}{24}(a + b + c + d) + \frac{1}{2}e((\delta_{i,j-1}^y)^2 + J_{i,j-1}^{y^2}) + \\
&\quad \frac{1}{2}f((\delta_{i,j+1}^y)^2 + J_{i,j+1}^{y^2}) + \frac{1}{2}g((\delta_{i+1,j-1}^y)^2 + J_{i+1,j-1}^{y^2}) + \\
&\quad \frac{1}{2}h((\delta_{i+1,j+1}^y)^2 + J_{i+1,j+1}^{y^2}) \\
\frac{\partial^2}{\partial x \partial y} &: 0 = e(\delta_{i,j-1}^x \delta_{i,j-1}^y + J_{i,j-1}^{xy}) + f(\delta_{i,j+1}^x \delta_{i,j+1}^y + J_{i,j+1}^{xy}) + \\
&\quad g(\delta_{i+1,j-1}^x \delta_{i+1,j-1}^y + J_{i+1,j-1}^{xy}) + h(\delta_{i+1,j+1}^x \delta_{i+1,j+1}^y + J_{i+1,j+1}^{xy}) \\
\frac{\partial^3}{\partial y^3} &: 0 = \frac{1}{6}e((\delta_{i,j-1}^y)^3 + 3\delta_{i,j-1}^y J_{i,j-1}^{y^2}) + \frac{1}{6}f((\delta_{i,j+1}^y)^3 + 3\delta_{i,j+1}^y J_{i,j+1}^{y^2}) + \\
&\quad \frac{1}{6}g((\delta_{i+1,j-1}^y)^3 + 3\delta_{i+1,j-1}^y J_{i+1,j-1}^{y^2}) + \frac{1}{6}h((\delta_{i+1,j+1}^y)^3 + 3\delta_{i+1,j+1}^y J_{i+1,j+1}^{y^2})
\end{aligned}$$

678

$$\begin{aligned}
\frac{\partial^3}{\partial x^2 \partial y} &: 0 = \frac{1}{2}e((\delta_{i,j-1}^x)^2 \delta_{i,j-1}^y + \delta_{i,j-1}^x J_{i,j-1}^{x^2}) + \frac{1}{2}f((\delta_{i,j+1}^x)^2 \delta_{i,j+1}^y + \delta_{i,j+1}^x J_{i,j+1}^{x^2}) + \\
&\quad \frac{1}{2}g((\delta_{i+1,j-1}^x)^2 \delta_{i+1,j-1}^y + \delta_{i+1,j-1}^x J_{i+1,j-1}^{x^2}) + \frac{1}{2}h((\delta_{i+1,j+1}^x)^2 \delta_{i+1,j+1}^y + \delta_{i+1,j+1}^x J_{i+1,j+1}^{x^2}) \\
\frac{\partial^3}{\partial x \partial y^2} &: 0 = \frac{1}{2}e(\delta_{i,j-1}^x (\delta_{i,j-1}^y)^2 + \delta_{i,j-1}^x J_{i,j-1}^{y^2}) \\
&\quad \frac{1}{2}f(\delta_{i,j+1}^x (\delta_{i,j+1}^y)^2 + \delta_{i,j+1}^x J_{i,j+1}^{y^2}) \\
&\quad \frac{1}{2}g(\delta_{i+1,j-1}^x (\delta_{i+1,j-1}^y)^2 + \delta_{i+1,j-1}^x J_{i+1,j-1}^{y^2}) \\
&\quad \frac{1}{2}h(\delta_{i+1,j+1}^x (\delta_{i+1,j+1}^y)^2 + \delta_{i+1,j+1}^x J_{i+1,j+1}^{y^2}).
\end{aligned}$$

679 Solving these equations by a least square method leads to zero values for e , f , g and h .

680 C. Computation of kinetic moments

681 This section presents the calculation of kinetic moment which are used in the formulation of inter-
 682 polation coefficients. Firstly, these moments are pre-computed in the general frame and geometrical
 683 transformations are then employed to obtain these moments in local frame. Unfortunately, this method
 684 suffers of round-off errors if the mesh is very-stretched, therefore the calculation of kinetic moments is
 685 done directly in local frame.

686 The coordinates in global frame are denoted as (x, y, z) , and as (x', y', z') for the local frame. Two
 687 kind of moments have to be calculated: cells and interfaces kinetic moments. Cells kinetic moments are
 688 denoted by $J^{x'm y'n z'p}$. Since the local coordinate x', y', z' could be expressed as linear function of x, y, z ,
 689 the calculation of kinetic moments consist simply of the numerical integration of polynomial function :

$$J^{x'm y'n z'p} = \frac{1}{|\Omega|} \int_{\Omega} \left[\underbrace{(a_{x'}a + b_{x'}y + c_{x'}z + d_{x'})^m}_{x'} \dots \underbrace{(a_{z'}x + b_{z'}y + c_{z'}z + d_{z'})^p}_{z'} \right] d\Omega = \frac{1}{|\Omega|} \int_{\Omega} P(x, y, z) d\Omega \quad (56)$$

690 where $P(x, y, z)$ represent a polynomial of order $n + m + p$ function of x, y, z .

691 The cell Ω is supposed to be defined only by its eight vertices, and a tri-linear transformation is applied
 692 to transform the physical cell Ω into the iso-parametric cell Ω^* defined by :

$$\Omega^* = \begin{cases} -1 \leq \xi \leq 1 \\ -1 \leq \eta \leq 1 \\ -1 \leq \zeta \leq 1 \end{cases}, \quad (57)$$

693 and the numerical integration is performed by a Gauss quadrature on Ω^* .

694 The position vector for a point inside the cell Ω can be expressed in terms of ξ, η and ζ by :

$$\begin{aligned} 8\vec{x} &= (1 - \xi)(1 - \eta)(1 - \zeta)\vec{x}_1 + (1 + \xi)(1 - \eta)(1 - \zeta)\vec{x}_2 + (1 - \xi)(1 + \eta)(1 - \zeta)\vec{x}_3 \\ &+ (1 + \xi)(1 + \eta)(1 - \zeta)\vec{x}_4 + (1 - \xi)(1 - \eta)(1 + \zeta)\vec{x}_5 + (1 + \xi)(1 - \eta)(1 + \zeta)\vec{x}_6 \\ &+ (1 - \xi)(1 + \eta)(1 + \zeta)\vec{x}_7 + (1 + \xi)(1 + \eta)(1 + \zeta)\vec{x}_8 \end{aligned} \quad (58)$$

695 where \vec{x}_i represent the vertices of Ω . Thus we obtain :

$$J^{x'm y'n z'p} = \frac{1}{|\Omega|} \int_{-1}^1 \int_{-1}^1 \int_{-1}^1 |Jac| P(\xi, \eta, \zeta) d\xi d\eta d\zeta \quad (59)$$

696 where $|Jac|$ denote the jacobian of the tri-linear transformation.

697 A Gaussian approximation is used for each integral :

$$J^{x'm y'n z'p} = \frac{1}{|\Omega|} \sum \sum \sum w_i w_j w_k |Jac| P(\beta_i, \beta_j, \beta_k) \quad (60)$$

698 where β_i represent the Gauss points and w_i the corresponding weight. As the highest order for kinetic
 699 moments integrands is five, the highest order is six for the function $|Jac|P$ and so three Gauss points

700 are used in each direction.

701 One can notice that the grid geometry can be approximated to a higher order by using a polynomial
702 transformation instead of a tri-linear ones. This possibility will be studied in the future.

703 For an interface kinetic moment, a parametrization of the interface is introduced as for the cell
704 moment and the formula :

$$\int_S f(x, y, z) dS = \int_{-1}^1 \int_{-1}^1 f(\xi, \eta) \|\vec{r}_\xi \vec{r}_\eta\| d\xi d\eta \quad (61)$$

705 is used to calculate the integral with a gaussian quadrature. In this formula, $\vec{r}(\xi, \eta)$ represent a point on
706 the surface S and the two vector \vec{r}_ξ and \vec{r}_η are calculated by :

$$\vec{r}_t = \left(\frac{\partial x}{\partial t}, \frac{\partial y}{\partial t}, \frac{\partial z}{\partial t} \right)^T \quad (62)$$

707 where t represents either ξ or η .

- 709 [1] Ashcroft, G., Zhang, X., 2003. Optimized prefactored compact schemes. *J. Comput. Phys.* 190 (2), 459–477.
- 710 [2] Cambier, L., Gazaix, M., Jan. 2002. elsA: an efficient object-oriented solution to CFD complexity. In: 40th AIAA
711 Aerospace Science Meeting and Exhibit, Reno. AIAA 2002-0108, pp. 14–17.
- 712 [3] Gaitonde, D. V., Shang, J. S., December 1997. Optimized compact-difference-based finite-volume schemes for linear
713 wave phenomena. *Journal of Computational Physics* 138 (2), 617–643.
- 714 [4] Gaitonde, D. V., Visbal, M. R., January 11-14 1999. Further development of a navier-stokes solution procedure based
715 on higher-order formulas. In: 37th Aerospace Sciences Meeting and Exhibit, Reno, Nevada. No. AIAA-1999-557.
- 716 [5] Gamet, L., Ducros, F., Nicoud, F., Poinso, T., 1999. Compact finite difference schemes on non-uniform meshes.
717 application to direct numerical simulations of compressible flows. *International Journal for Numerical Methods in*
718 *Fluids* 29, 159–191.
- 719 [6] Gloerfelt, X., Novembre 2001. Bruit Rayonné par un Écoulement Affleurant une Cavité: Simulation Aéroacoustique
720 Directe et Application de Méthodes Intégrales. Ph.D. thesis, Laboratoire de Mécanique de Fluides et d'Acoustique,
721 UMR CNRS 5509, Ecole Centrale de Lyon.
- 722 [7] Gottlieb, S., Chi-Shu, W., 1996. Total variation diminishing runge-kutta schemes. Tech. rep., Institute for Computer
723 Applications in Science and Engineering (ICASE).
- 724 [8] Gustafsson, B., 1975. The convergence rate for difference approximations to mixed initial boundary value problems.
725 *Mathematics of Computations* 29 (130), 396–406.
- 726 [9] Hardin, J. C., Ristorcelli, J. R., Tam, C. K. W. (Eds.), October 24-26 1994. ICASE/LaRC Workshop on Benchmark
727 Problems in Computational Aeroacoustics (CAA). NASA and ICASE, Hampton, Virginia.
- 728 [10] Hixon, R., December 2000. Prefactored small-stencil compact schemes. *Journal of Computational Physics* 165 (2),
729 522–541.
- 730 [11] Jameson, A., Schmidt, W., Turkel, E., 1981. Numerical Solutions of the Euler Equations by Finite Volume Methods
731 Using Runge-Kutta Time-Stepping Schemes. In: AIAA 14th Fluid and Plasma Dynamic Conference. No. AIAA Paper
732 81-1259. Palo Alto.
- 733 [12] Kobayashi, M. H., 1999. On a class of padé finite volume methods. *Journal of Computational Physics* 156 (1), 137–180.
- 734 [13] Lacor, C., Smirnov, S., Baelmans, M., 2004. A finite volume formulation of compact schemes on arbitrary structured
735 grids. *Journal of Computational Physics* 198, 535–566.
- 736 [14] Lele, S. K., 1992. Compact finite difference schemes with spectral-like resolution. *Journal of Computational Physics*
737 103, 16–42.
- 738 [15] Mattiussi, C., May 1997. An analysis of finite volume, finite element, and finite difference methods using some concepts
739 of algebraic topology. *Journal of Computational Physics* 133 (2), 289–309.
- 740 [16] Nance, D. V., Viswanathan, K., Sankar, L. N., February 1997. Low-dispersion finite volume scheme for aeroacoustic
741 applications. *AIAA Journal* 35 (2), 255–262.
- 742 [17] Pereira, J. M. C., Kobayashi, M. H., Pereira, J. C. F., February 2001. A fourth-order-accurate finite volumenext term
743 compact method for the incompressible navier-stokes solutions. *Journal of Computational Physics* 167 (1), 217–243.
- 744 [18] Piller, M., Stalio, E., 2004. Finite-volume compact schemes on staggered grids. *Journal of Computational Physics*
745 197 (1), 299–340.
- 746 [19] Piller, M., Stalio, E., 2008. Compact finite volume schemes on boundary-fitted grids. *Journal of Computational Physics*
747 227 (9), 4736–4762.
- 748 [20] Poinso, T. J., Lele, S. K., Jul. 1992. Boundary conditions for direct simulations of compressible viscous flows. *Journal*
749 *of Computational Physics* 101, 104–129.
- 750 [21] Popescu, M., Shyy, W., Garbey, M., 2005. Finite volume treatment of dispersion-relation-preserving and optimized
751 prefactored compact schemes for wave propagation. *Journal of Computational Physics* 210 (2), 705–729.
- 752 [22] Sengupta, T. K., Ganerwal, G., De, S., 2003. Analysis of central and upwind compact schemes. *Journal of Computa-*
753 *tional Physics* 192, 677–694.
- 754 [23] Tam, C. K. W., October 1995. Computational aeroacoustics: Issues and methods. *AIAA Journal* 33 (10), 1788–1796.

- 755 [24] Tam, C. K. W., Dong, Z., 1996. Radiation and outflow boundary conditions for direct computation of acoustic and
756 flow disturbances in a nonuniform mean flow. *Journal of Computational Acoustics* 4 (2), 175–201.
- 757 [25] Tam, C. K. W., Webb, J. C., August 1993. Dispersion-relation-preserving finite difference schemes for computational
758 acoustics. *Journal of Computational Physics* 107 (2), 262–281.
- 759 [26] Visbal, M. R., Gaitonde, D. V., September 2002. On the use of higher-order finite-difference schemes on curvilinear
760 and deforming meshes. *Journal of Computational Physics* 181 (1), 155–185.